

# Bioprinted 3D Outer Retina Barrier Uncovers RPE-dependent Choroidal Phenotype in Advanced Macular Degeneration

**Kapil Bharti** (✉ [kapil.bharti@nih.gov](mailto:kapil.bharti@nih.gov))

Ocular and Stem Cell Translational Research Section, National Eye Institute, National Institutes of Health, Bethesda, MD 20892

**Min Jae Song**

National Center for Advancing Translational Sciences, National Eye Institute, National Institutes of Health, National Institutes of Health

**Russell Quinn**

National Eye Institute, National Institutes of Health

**Eric Nguyen**

National Eye Institute, National Institutes of Health <https://orcid.org/0000-0002-4164-5548>

**Tea Soon Park**

National Eye Institute, National Institutes of Health

**Christopher Hampton**

National Eye Institute, National Institutes of Health

**Ruchi Sharma**

Unit on Ocular and Stem Cell Translational Research, National Eye Institute, National Institutes of Health

**Céline Koster**

Department of Clinical Genetics, Amsterdam University Medical Centers (AUMC), Location Academic Medical Center (AMC), University of Amsterdam (UvA)

**Ty Voss**

National Center for Advancing Translational Sciences

**Carlos Tristan**

National Center for Advancing Translational Sciences

**Claire Malley**

NIH National Center for Advancing Translational Sciences <https://orcid.org/0000-0002-2352-8479>

**Anju Singh**

National Center for Advancing Translational Sciences, National Institutes of Health

**Roba Dejene**

National Eye Institute, National Institutes of Health

**Devika Bose**

National Eye Institute, National Institutes of Health

**Paige Derr**

NIH

**Kristy Derr**

NIH

**Sam Michael**

National Center for Advancing Translational Sciences

**Francesca Barone**

National Eye Institute, National Institutes of Health

**Arvydas Maminishkis**

National Eye Institute, National Institutes of Health

**Ilyas Singec**

NCATS/NIH

**Marc Ferrer**

NCATS, NIH

---

**Article**

**Keywords:**

**Posted Date:** January 13th, 2021

**DOI:** <https://doi.org/10.21203/rs.3.rs-135775/v1>

**License:**  This work is licensed under a Creative Commons Attribution 4.0 International License.

[Read Full License](#)

---

1 **Bioprinted 3D Outer Retina Barrier Uncovers RPE-dependent Choroidal Phenotype in Advanced**  
2 **Macular Degeneration**

3 Min Jae Song<sup>1,2</sup>, Russ Quinn<sup>1</sup>, Eric Nguyen<sup>1</sup>, Christopher Hampton<sup>1</sup>, Ruchi Sharma<sup>1</sup>, Tea Soon Park<sup>1</sup>,  
4 Céline Koster<sup>3</sup>, Ty Voss<sup>2</sup>, Carlos Tristan<sup>2</sup>, Claire Malley<sup>2</sup>, Anju Singh<sup>2</sup>, Roba Dejene<sup>1</sup>, Devika Bose<sup>1</sup>, Paige  
5 Derr<sup>2</sup>, Kristy Derr<sup>2</sup>, Sam Michael<sup>2</sup>, Francesca Barone<sup>1</sup>, Arvydas Maminishkis<sup>1</sup>, Ilyas Singec<sup>2</sup>, Marc Ferrer<sup>2</sup>,  
6 Kapil Bharti\*<sup>1,2</sup>

7 <sup>1</sup>National Eye Institute, National Institutes of Health

8 <sup>2</sup>National Center for Advancing Translational Sciences, National Institutes of Health

9 <sup>3</sup>Department of Clinical Genetics, Amsterdam University Medical Centers (AUMC), Location  
10 Academic Medical Center (AMC), University of Amsterdam (UvA), 1105 AZ Amsterdam, The  
11 Netherlands.

12 **Keywords:** Age-related macular degeneration, choroidal neovascularization, engineered vascular-outer-  
13 blood-retina-barrier, retinal pigment epithelium, Bruch's membrane, choriocapillaris

14

15

16

17

18

19

20

21

22

23

24 **Abstract**

25 Age-related macular degeneration (AMD), a leading cause of blindness, initiates in the outer-blood-retina-  
26 barrier (oBRB) formed by Retinal pigment epithelium (RPE), Bruch's membrane, and choriocapillaris. The  
27 mechanism of AMD initiation and progression remain poorly understood due to the lack of physiologically  
28 relevant oBRB models. We engineered a native-like 3D-oBRB tissue by bioprinting endothelial cells,  
29 pericytes, and fibroblasts on the basal side of a biodegradable scaffold and establishing an RPE monolayer  
30 on top. In this 3D-oBRB, a fully-polarized RPE monolayer with apical processes and basal infoldings  
31 provides barrier resistance, induces fenestration and choroid-specific gene expression in the  
32 choriocapillaris, and supports the formation of a Bruch's-like membrane that allows tissue integration in  
33 rat eyes. Complement activation in the 3D-oBRB triggers dry-AMD phenotypes (including subRPE drusen  
34 and choriocapillaris degeneration), and hypoxia activated HIF- $\alpha$  induces wet-AMD phenotypes  
35 (choriocapillaris neovascularization). Anti-VEGF drug treatment suppresses neovascularization -  
36 validating this model for clinical translation and drug discovery.

37

38

39

40

41

42

43

44

45

## 46 **Introduction**

47 Age-related macular degeneration (AMD) affects over 196 million people worldwide and leads to blindness  
48 in advanced stages<sup>1</sup>. Atrophy of the retinal pigment epithelium (RPE) and the choriocapillaris of the choroid  
49 in advanced AMD stages trigger photoreceptor cell death leading to blindness<sup>2,3</sup>. With its functional tight  
50 junctions, the RPE monolayer and the choriocapillaris, separated by a proteinaceous (2-5  $\mu\text{m}$  thick) Bruch's  
51 membrane, form the outer-blood-retina-barrier (oBRB) in the back of the eye<sup>4</sup>. RPE basal infoldings,  
52 Bruch's membrane, and fenestrations (60-80 nm pores) in the endothelial cell (EC) membrane allow  
53 unimpeded macromolecule and nutrient flow from the blood into the RPE - which regulates flow to the  
54 photoreceptors<sup>4</sup>.

55 Dry AMD initiates by the accumulation of lipid/protein-rich drusen deposits, triggered by complement  
56 pathway activation, in the subRPE region<sup>3,4</sup>. Disease progression to the advanced stage geographic atrophy  
57 is hallmarked by RPE dropout that precedes choriocapillaris degeneration, leading to outer retina starvation<sup>3</sup>.  
58 In contrast, in advanced wet AMD (choroidal neovascularization, CNV) choriocapillaris hyperproliferate,  
59 grow under the RPE and occasionally break through RPE tight junctions leaking blood in the sub-retinal  
60 space<sup>5</sup>. This separates the photoreceptors from the RPE and deprives them of the RPE's functional and  
61 nutrient support resulting in photoreceptor degeneration<sup>5</sup>. The importance of vascular endothelial growth  
62 factor (VEGF) in CNV is underscored by the successful application of drugs that block VEGF signaling  
63 (Bevacizumab, Ranibizumab, and Aflibercept)<sup>6,7</sup>. However, the mechanism of increased VEGF secretion  
64 by human RPE remains elusive due to a lack of human-relevant models that accurately recapitulate CNV.  
65 Here, we developed a functionally validated 3D-oBRB utilizing bioprinting, tissue engineering, and  
66 directed differentiation of human induced pluripotent stem cells (iPSCs). The 3D-oBRB model recapitulates  
67 RPE-choriocapillaris interactions under healthy and dry and wet AMD stages.

68

69

70 **Results**

71 **Design of 3D outer blood-retina barrier (3D-oBRB)**

72 To develop a functional 3D-oBRB, we included the four key cell types (RPE, ECs, pericytes, and fibroblasts)  
73 in our tissue design (Fig. 1a)<sup>8,9</sup>. The identity of iPSC-derived ECs (iECs), iPSC-derived RPE (iRPE),  
74 primary ECs, pericytes, and fibroblasts was confirmed using cell type-specific markers (CD31, ETV2, vWF  
75 – ECs; NG2, PDGFR- $\beta$ , COL-I – pericytes; VIMENTIN, COL-I, PDGFR- $\beta$  (negative) – fibroblasts; MITF,  
76 TYRP1, ZO-1, RPE65, EZRIN – RPE, Fig. S1)<sup>10-12</sup>. A biodegradable scaffold made of thermally fused  
77 electrospun poly-(lactic-co-glycolic acid) (PLGA) fibers of 400-500 nm diameter supported the formation  
78 of a polarized RPE monolayer on one side and a capillary-bed derived from 3D-printed bioink of ECs,  
79 pericytes, and fibroblasts on the other side (Figs. 1a and S2a,b). As the tissue matured, the degrading  
80 scaffold was gradually replaced by extracellular matrix (ECM) secreted by RPE and ECs forming a Bruch's  
81 membrane-like structure between the RPE and the capillary-bed.

82 Manufacturing and functional maturation of the 3D-oBRB took 42 days (Fig. 1a). The printing surface was  
83 prepared a day before bioprinting by replacing the snapwell membrane with a 12 mm PLGA scaffold disc  
84 (Fig. 1a; methods). The scaffold's RPE side was coated with vitronectin (50 $\mu$ g/mL) to aid cell attachment.  
85 To enhance scaffold hydrophilicity - needed for bioink attachment, scaffold was treated with oxygen plasma  
86 (5cc/min, 30mins). Improved hydrophilicity was confirmed by the dispersal of a water droplet (Figs. 1a,  
87 S2c, d).

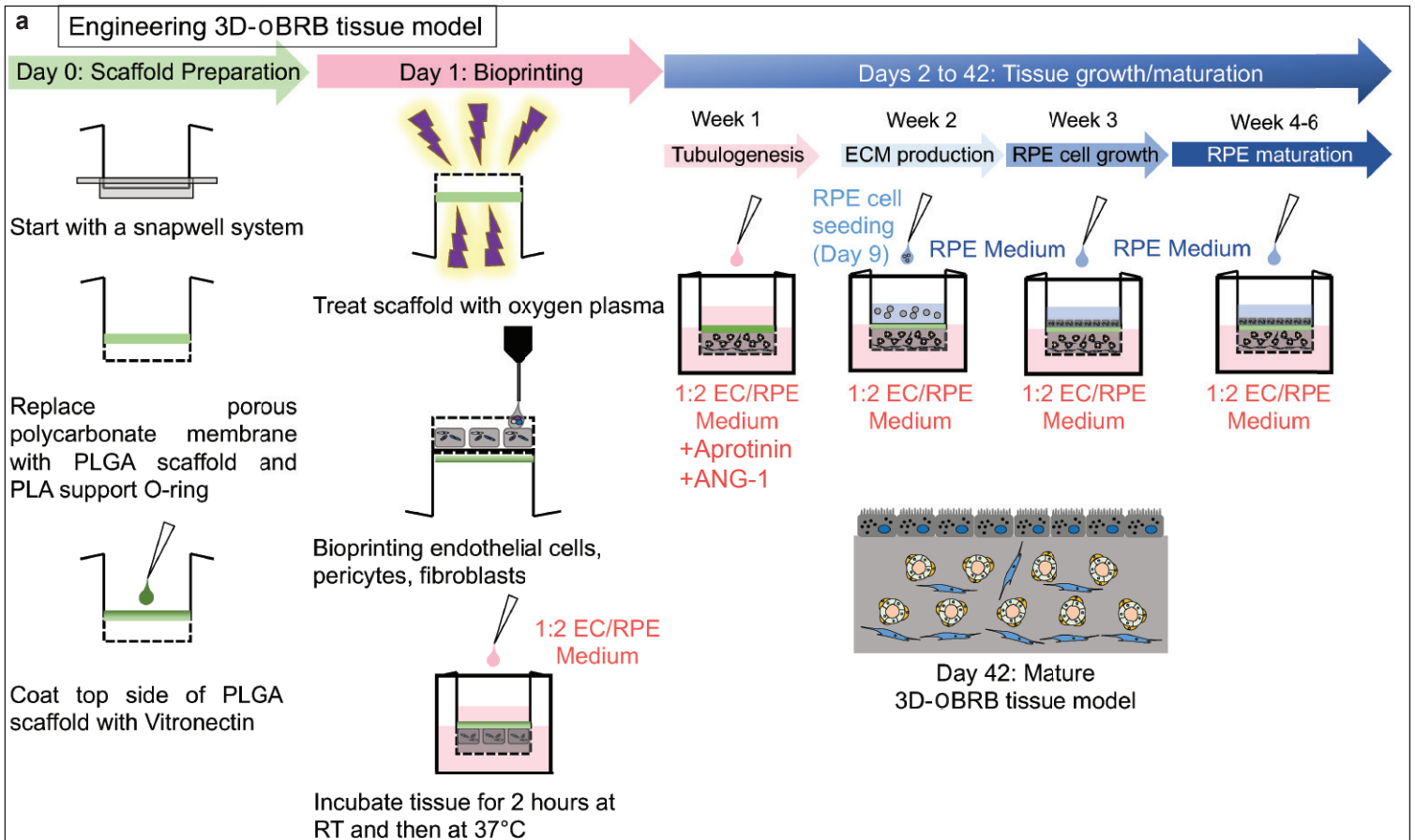
88

89

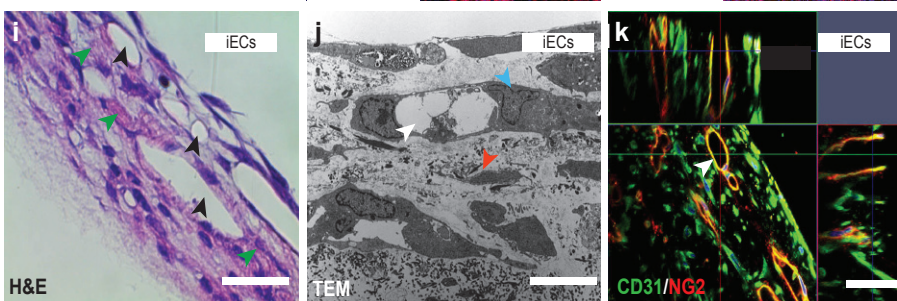
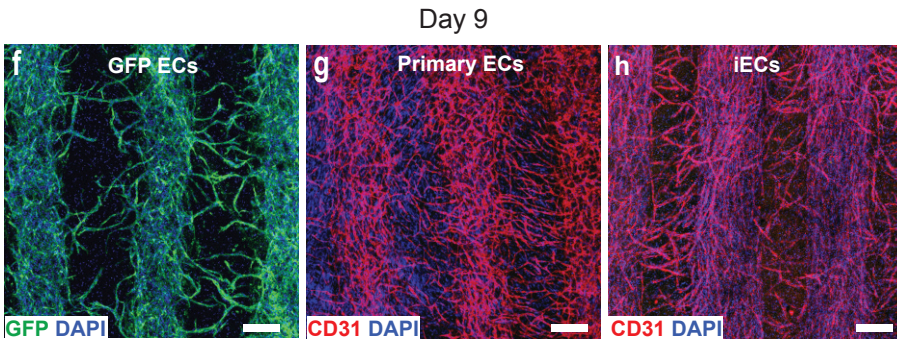
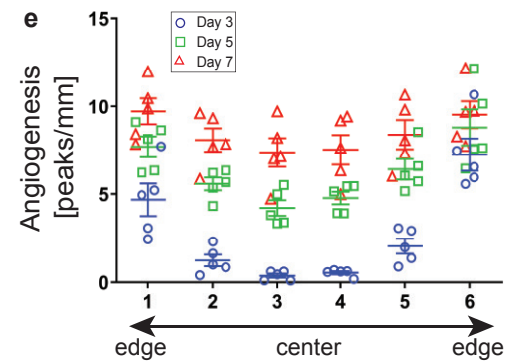
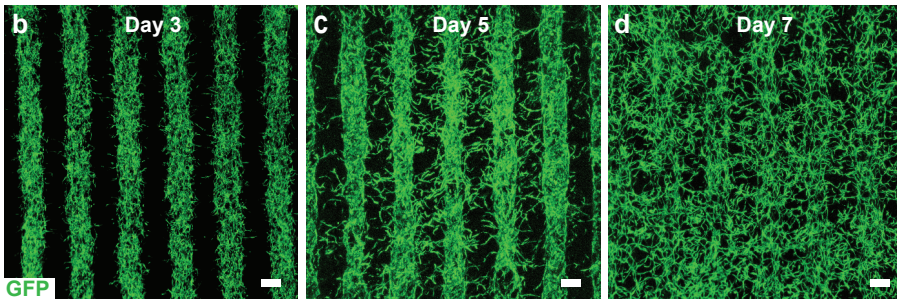
90

91

92



GFP-ECs



93 **Fig. 1 | Design of 3D-oBRB.** a, Bioprinting workflow with human endothelial cells (ECs) and RPE. **b-d**,  
94 Vascular development of GFP expressing primary ECs on day 3 (**a**), day 5 (**b**) and day 7 (**c**) after printing.  
95 Scale bars, 500  $\mu\text{m}$ . **e**, Angiogenesis between printed stripes (n=5). #p<0.05 in day 3 vs. day 5, †p<0.05 in  
96 day 5 vs. day 7, \*p<0.05 in day 3 vs. day 7. **f-h**, Vascular formation of GFP-positive ECs (green, **f**), primary  
97 ECs (CD31 - red, **g**), and iPSC-derived ECs (iECs, CD31 – red, **h**) and nuclei (blue). Scale bars, 500  $\mu\text{m}$ .  
98 **i**, H&E images of 10  $\mu\text{m}$  thick cross section of iECs derived vascular tissue (day 7). Vasculature is marked  
99 with black arrowheads, and ECM components are marked with green arrowheads. Scale bar, 50  $\mu\text{m}$ . **j**,  
100 Transmission electron microscope (TEM) images of iECs derived vascular tissue at day 7. White arrowhead  
101 shows a capillary, blue arrowhead marks pericytes, and red arrowhead labels fibroblasts. Scale bar, 300 nm.  
102 **k**, Orthogonal views of confocal images of 100  $\mu\text{m}$  thick tissue sections stained with CD31 (ECs; green)  
103 and NG2 (pericytes; red). White arrowheads mark patent EC-derived capillaries. Scale bar, 50  $\mu\text{m}$ .  
104 Statistical significance was attributed to values of p<0.05 as determined by two-way ANOVA and  
105 Bonferroni post-hoc pair comparison. All error bars indicate STE.

106

107

108

109

110

111

112

113

114

## 115 **Engineering 3D capillary-bed**

116 To produce a dense capillary-bed of 5-20 $\mu$ m lumen diameter<sup>13</sup>, we sought to bioprint a high density of  
117 mixed ECs, pericytes and fibroblasts (12/6/0.6 million fibroblasts/EC's/pericytes per mL of bioink). To  
118 achieve a homogenous bioink with such high cell density, we designed a temperature-sensitive hydrogel by  
119 mixing a gelatin-based hydrogel (Novogel, 60 mg/mL) with fibrinogen (2.5mg/mL) at 37°C reduced  
120 hydrogel viscosity allowing bioink homogeneity and easier loading in the printing syringe. Cooling the  
121 syringe down to 10°C increased bioink viscosity allowing for easy printing of desired structures. During  
122 tissue culture at 37°C, Novogel dissolved and fibrin continued to provide the 3D architecture needed to  
123 support capillary-bed formation. However, fibrin degraded after four days leading to capillary-bed collapse,  
124 as confirmed by the clumping of GFP-expressing ECs (Figs. S3a,b). The addition of recombinant aprotinin  
125 (25 $\mu$ g/mL), a known fibrinolysis inhibitor, prevented tissue collapse giving fibroblasts time to secrete ECM  
126 that enabled a stable capillary network (Figs. S3c,d).

127

128 A striped bioprinting pattern facilitated capillary growth quantification outwards from the printed stripes  
129 into the acellular hydrogel (movie S1; Fig. S4). A MATLAB-based algorithm was developed for  
130 angiogenesis quantification (Methods). Bioprinted tissue was treated with VEGF (85ng/mL) for three or  
131 seven days, to determine the optimal treatment window for capillary growth. Capillary sprouting was  
132 evident in printed ECs with three-days of VEGF treatment, but these sprouts did not form a contiguous  
133 capillary-network and disintegrated by day 7 (arrowheads, Fig. S4a). In comparison, seven-days treatment  
134 increased capillary angiogenesis resulting in anastomosis between two printed stripes (arrowheads, Fig.  
135 S4b, movie S1). Quantification revealed 1.5-2x folder higher angiogenesis on the edges of the printed  
136 tissues and 5-10x fold more angiogenesis in the center of the acellular structure after seven-days VEGF  
137 treatment as compared to three-days treatment (Figs. S4a-e), establishing the use of exogenous VEGF for  
138 seven days.

139 Exogenous VEGF treatment supported EC angiogenesis, but it also increased EC migration resulting in  
140 sole ECs that didn't incorporate into capillaries<sup>14</sup> (Figs. S5a and b - circle). To prevent this undesirable EC  
141 migration, we supplemented tissues with recombinant angiopoietin-1 (ANG-1; 100 ng/mL), a well-known  
142 EC migration inhibitor. Expectedly, ANG-1 initially slowed down capillary sprouting (arrowheads Figs.  
143 S5a and c), but it did not disrupt capillary formation. In fact, by day 8 the number of capillaries increased  
144 in ANG-1 treated Group 2 as compared to without it (Group 1) (Figs. S5 b,d). This allowed more precise  
145 analysis of the angiogenesis kinetics excluding individual EC signal.

146

147 To monitor the time course of angiogenesis, we analyzed the GFP-expressed ECs on days 3, 5 and 7 post-  
148 printing. By day 3, capillaries grew in a gradient with 5-6 capillary peaks/mm close to the printed stripe  
149 edge the and no peaks in the center of the acellular zone ( $p < 0.001$ ; Figs. 1b, e, S6a). By day 5, the capillary  
150 gradient between stripe edges and the acellular area center was shallowed with 8 peaks/mm on edges and 4  
151 peaks/mm in the center ( $p < 0.05$ ; Figs. 1c, e, S6b). By day 7, no statistically significant difference between  
152 edges (9 peaks/mm) and center (10 peaks/mm) was evident ( $p > 0.05$ ; Figs. 1d, e, S6c). A comparative  
153 analysis of capillary networks derived from GFP-expressing ECs, non-GFP expressing ECs, and iECs  
154 revealed similar capillary confluency and angiogenesis throughout the tissue (Figs. 1f-h). Together, this  
155 confirmed robustness of our bioprinting protocol across different ECs. Histological analysis (H&E staining)  
156 of tissue sections confirmed capillaries with 5-20 $\mu$ m lumen diameters (black arrowheads) and interstitial  
157 spaces filled with cells and ECM (green arrowheads; Fig. 1i). Transmission electron microscopy (TEM) of  
158 tissue cross-sections confirmed iECs derived capillaries (white arrowhead) with a pericyte (blue arrowhead)  
159 wrapped around, and fibroblasts (red arrowhead) in interstitial spaces (Fig. 1j). This observation was further  
160 confirmed in confocal images of 100 $\mu$ m thick tissue slices where pericytes (NG2, red) were found to  
161 colocalize with iEC (CD31, green) derived intact capillaries (arrowhead; Fig. 1k, movie S2). Overall, this  
162 data shows that our bioink composed of Novogel, fibrinogen mixed with fibroblasts, ECs, and pericytes  
163 (2:1:0.1 ratio) forms a robust capillary-network with both primary and iPSC-ECs.

## 164 **Development of 3D-oBRB**

165 To complete the 3D-oBRB, iPSC-derived RPE cells were seeded and matured<sup>12</sup> on the Vitronectin-coated  
166 scaffold side. TEM confirmed iRPE cells-initiated polarization and pigmentation within three weeks after  
167 seeding (Fig. 2a). By six weeks, known structural features of RPE maturation and polarization were evident:  
168 dense apical processes (ap), tight junctions (tj) between neighboring cells, apically located stage IV  
169 melanosomes (ml), and basal infoldings (bi) - a critical native-RPE feature that cannot be reproduced in  
170 RPE grown on plastic substrates<sup>15</sup> (Fig. 2b). Similar to the native-BRB, RPE basal infoldings were in  
171 continuum with the ECM that had replaced the scaffold and formed a Bruch's membrane (BM)-like  
172 structure (Fig. 2b)<sup>16</sup>. Immunostaining for the tight junction marker E-CADHERIN and the apical process  
173 marker EZRIN further confirmed RPE monolayer junctional maturity and polarization (Fig. 2c). Concurrent  
174 with the RPE maturation, capillary confluency was evident in CD31 immunostained 3D rendered tissue  
175 images (Fig. 2d). High expression of FELS, a fenestration marker<sup>17</sup>, colocalized with CD31 suggested the  
176 formation of fenestration in our 3D-oBRB model (Fig. 2e, movie S3). Histological analysis revealed the  
177 structure of the entire 3D-oBRB with a 2-4 $\mu$ m thick BM-like acellular ECM region sandwiched between  
178 an RPE monolayer on top and a 40-50 $\mu$ m thick vascular tissue with capillaries (cl) running along various  
179 tissue planes (Fig. 2f). To confirm functionality of the 3D-oBRB tight junctions, we measured tissue  
180 resistance to current flow (trans-epithelial resistance - TER), produced by functional tight junctions between  
181 neighboring RPE cells. TER of the tissue with vasculature and no iRPE layer was 53.4 ( $\pm$  1.36) Ohms $\cdot$ cm<sup>2</sup>.  
182 The presence of the iRPE monolayer increased the tissue TER to 740.4 ( $\pm$  155.99) Ohms $\cdot$ cm<sup>2</sup>, comparable  
183 to the TER of iRPE monolayer without the vascularized tissue 873.7 ( $\pm$  67.82) Ohms.cm<sup>2</sup> (Fig. 2g). Finally,  
184 to confirm capillaries' functionality in this 3D-oBRB, we transplanted the intact tissue in the choroid of  
185 immunocompromised rats. Two weeks post-transplantation, animals were perfused with DiI in the left heart  
186 ventricle to label all the vessels; and choroid was analyzed histologically. Anti-human STEM121 labeling  
187 with GFP-expressed ECs in 10 $\mu$ m cryosections identified human capillaries perfused with DiI suggesting  
188 anastomosis and integration with rat capillaries (Fig. 2h). This was further confirmed by 100 $\mu$ m sections

189 that revealed different size human capillaries anastomosed and integrated within rat capillaries (Figs. 2i,  
190 S7a, b). Overall, TEM, immunostaining, barrier resistance, and transplantation confirmed the formation of  
191 a functional 3D-oBRB with polarized RPE monolayer and functionally lumenized capillaries.

192

193

194

195

196

197

198

199

200

201

202

203

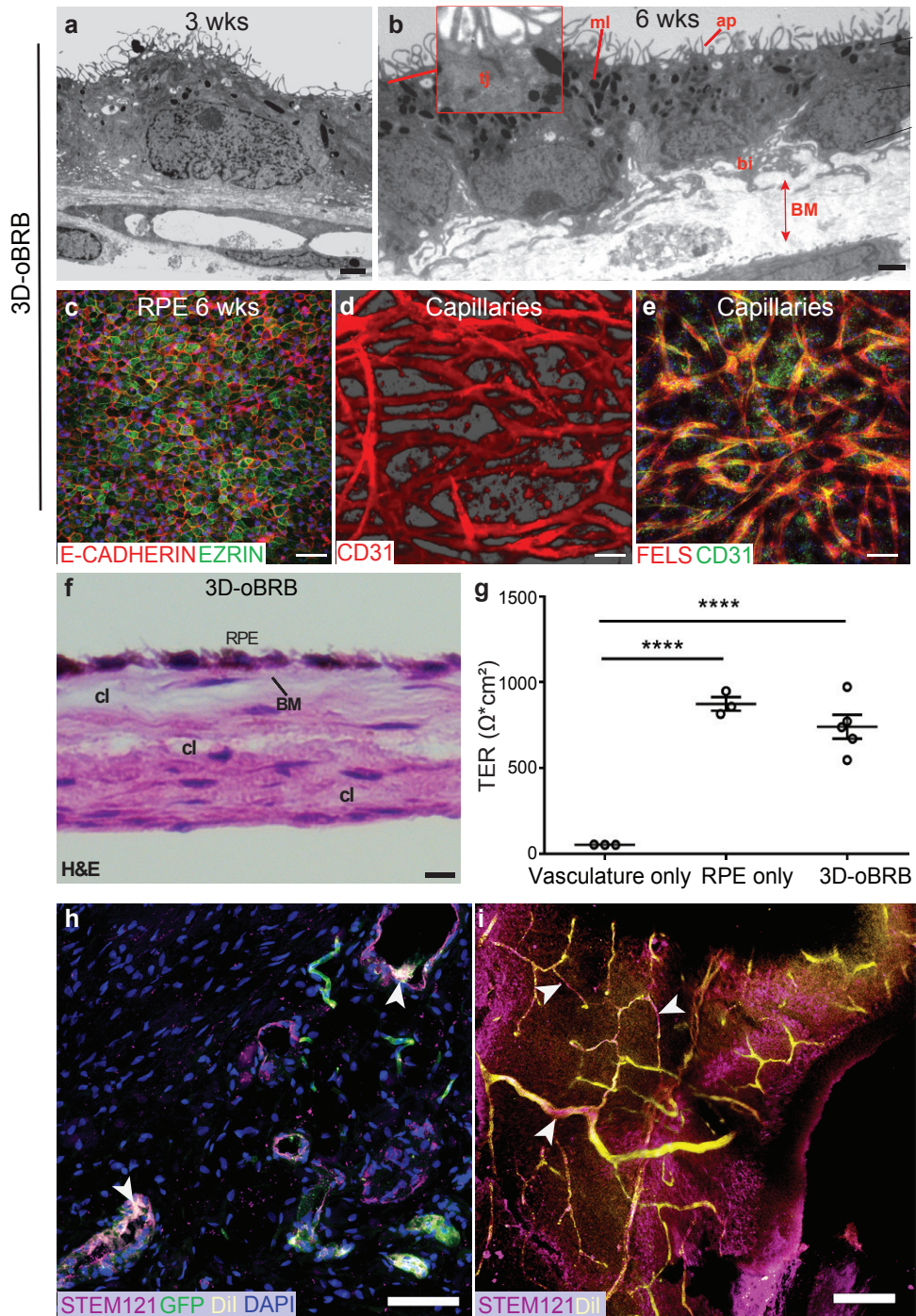
204

205

206

207

208



209 **Fig. 2 | Engineering of 3D oBRB. a,b**, TEM images of 3D-oBRB maturity at week 3 (**a**) and 6 (**b**) with  
210 RPE pigmentation: melanin (ml), RPE apical processes (ap), RPE basal infoldings (bl), tight junction (tj)  
211 formation and Bruch's membrane (BM). Scale bars, 1  $\mu\text{m}$  (**a**), 2  $\mu\text{m}$  (**b**) (n=3) **c**, Immunostaining for RPE  
212 maturity markers E-CADHERIN (red) and EZRIN (green) in 6-week-old tissues. Scale bar, 50  $\mu\text{m}$ . **d**, 3D-  
213 rendered image of CD31 (red) immunostained capillary-bed in 6-week-old 3D-oBRB. Scale bar, 50 $\mu\text{m}$ .  
214 (n=4) **e**, Immunostaining for capillary-maturation marker FELS (red) co-labeled with EC marker CD31  
215 (green) of confocal images of vascular networks labeled with CD31 (red). Scale bar, 50 $\mu\text{m}$ . (n=3) **f**, H&E  
216 staining of 6-week-old tissues containing capillaries (cl), RPE, and Bruch's membrane (BM). Scale bar, 10  
217  $\mu\text{m}$ . **g**, Transepithelial resistance (TER) of 3D-oBRB compared to vascular and 2D-RPE (n=3). **h**, GFP  
218 signal in human ECs and immunostaining with STEM121 (magenta) detect human capillaries that are  
219 perfused with DiI (yellow) in 10  $\mu\text{m}$  cryosections of rat choroid transplanted with 3D-oBRB. Scale bar 75  
220  $\mu\text{m}$ . (n=8 eyes from 4 animals). **i**, Immunostaining for STEM121 (magenta) detects human capillaries  
221 integrated with rat capillaries detected by Dil (yellow) perfusion in 100  $\mu\text{m}$  vibratome sections of  
222 transplanted rat choroid. Scale bar 100  $\mu\text{m}$ . Statistical significance was attributed to values of  $p < 0.05$  as  
223 determined by one-way ANOVA with Tukey's multiple-comparisons test. \*\*\*\* $p < 0.0001$ , All error bars  
224 indicate STE.

225

226

227

228

229

230

231

## 232 RPE cells induce capillary fenestration in 3D-oBRB

233 Strong FELS expression in fully-mature 3D-oBRB (Fig. 2e) suggested the presence of fenestration in  
234 capillaries. To better characterize the fenestration process, we performed a temporal analysis of FELS  
235 expression in 3D-oBRB constructs (Figs. S8a-d). CD31 co-immunostaining revealed minimal FELS  
236 expression in capillaries for the first two weeks post-printing (Figs. S8a, b). Coincidental with iRPE  
237 monolayer polarization (Fig. 2a), FELS expression became prominent starting week three (Figs. S8c, d).  
238 To confirm if FELS expression led to fenestration in fully-mature 3D-oBRB, we performed ultrastructural  
239 analysis of capillaries (Figs. 3a, b). TEM revealed 50-80 nm thinned areas in the EC capillary membrane  
240 reminiscent of fenestration in native choroidal capillaries (arrowheads Fig. 3b)<sup>18</sup>. To further confirm if  
241 FELS expression was affected by the RPE presence, we cultured the vascular tissue with (Figs. 3c, d, g) or  
242 without the RPE (Figs. 3e, f, g). CD31 and FELS co-immunostaining revealed a confluent capillary bed  
243 with higher capillary number and thickness, and a 2.5-fold higher FELS expression in tissues that contained  
244 the RPE as compared to tissues that lacked the RPE monolayer where vasculature collapsed (Figs. 3d, f, g).  
245 Overall, this work provides the first direct evidence that human RPE cells induce fenestration in an iEC-  
246 derived capillary-network.

247

248 RPE-dependent fenestration formation in our 3D-oBRB suggested that iECs acquire a choroidal fate. To  
249 investigate this possibility, we compared the transcriptome profiles of iECs within the 3D-oBRB and 2D  
250 monocultures (without RPE) using scRNAseq. Clustering samples by t-distributed stochastic neighbor  
251 embedding (tSNE) plots revealed three different EC populations in the 3D-oBRB, likely based on location  
252 in the tissue: fully-mature (FM) ECs expressed several choroidal and arterial maturation genes; partially-  
253 mature (PM) ECs expressed fewer arterial maturation genes; and inflamed (Inf) ECs expressed  
254 inflammatory genes in addition to arterial maturation genes (Figs. 3h,i, Table S3). Detailed analysis  
255 revealed genes relevant for ECM (*COL3A1*, *COL6A1*, *COL1A1*), EC maturation (*LOX*, *VEGFA*, *GJA4*,  
256 *ACE*), choroidal phenotype (*APOE*, *PLVAP*, *TIMP1*), angiogenesis (downregulated - *ENG*, *ACTB*, *MMP1*;

257 upregulated - *ADAM17*, *ITGAV*), and arterial maturation (*EPSA1*, *KDR*, *EFNB2*, and *NOTCH1*) showed  
258 the most differential expression among the 531 genes that were significantly different between 2D and 3D  
259 iEC transcriptomes (Figs. 3i, S9, S10)<sup>19-23</sup>. Overall, these findings suggest that our 3D-oBRB construct  
260 capillaries matured and attained an arterial and choroidal phenotype.

261

262

263

264

265

266

267

268

269

270

271

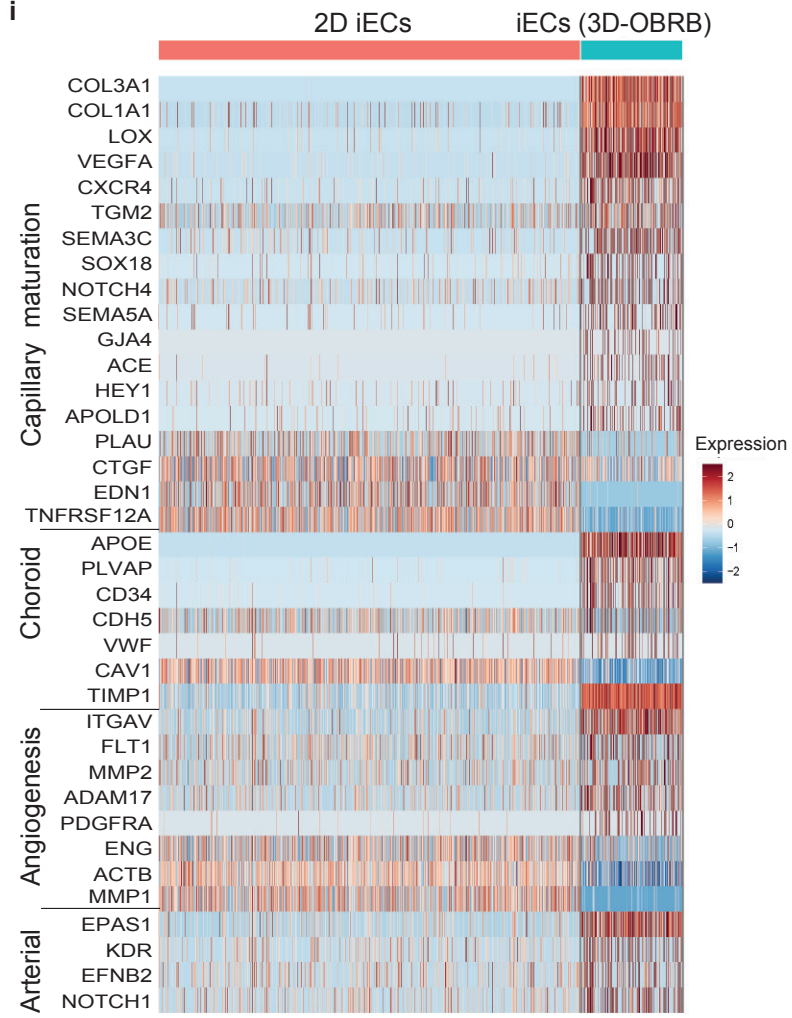
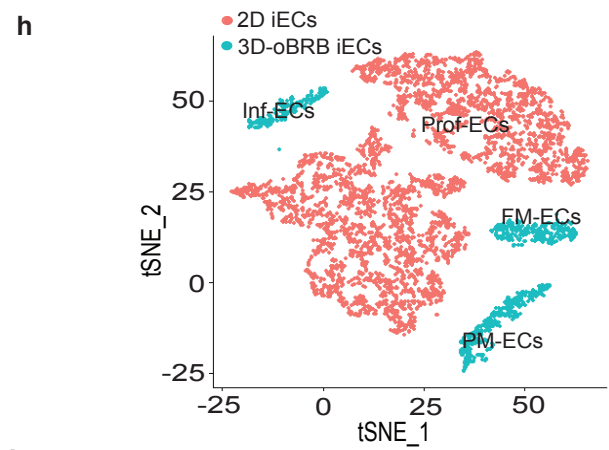
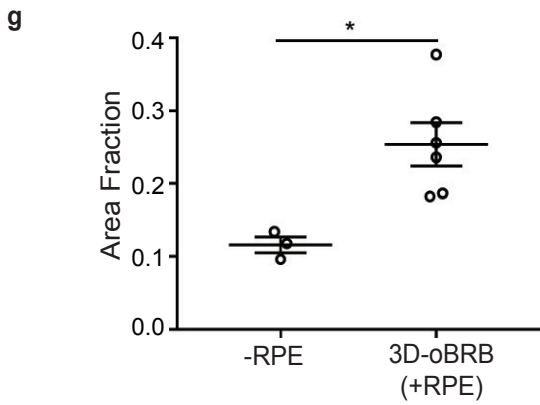
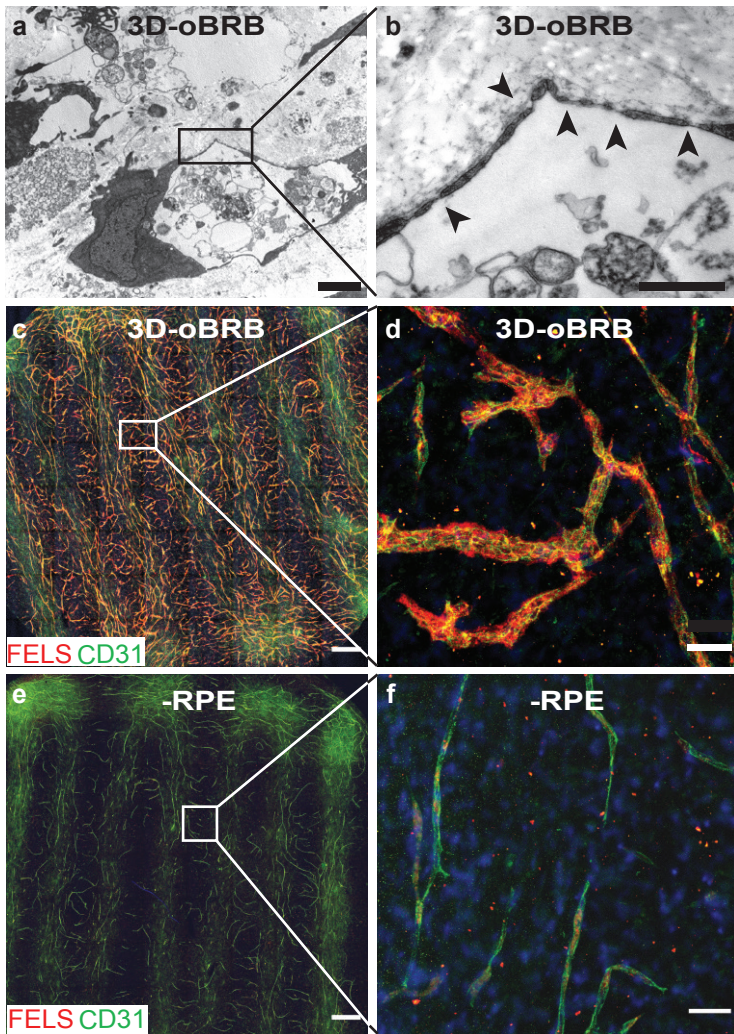
272

273

274

275

276



277 **Fig. 3 | Capillary maturation in 3D-oBRB. a,b,** TEM images highlight fenestration (arrowheads) in iECs  
278 with in 3D-oBRB capillaries at week 6. Scale bars, 2 $\mu$ m (**a**), 500nm (**b**). (n=3). **c-f,** Immunostaining for  
279 FELS (red) and CD31 (green) in 3D-oBRB (with RPE; **c, d**) or just the vasculature (without RPE; **e, f**).  
280 Scale bars, 500  $\mu$ m (**c, e**) and 50  $\mu$ m (**d, f**). **g,** Area fraction of FELS and CD31 expression in vascular  
281 regions with or without RPE. (n=3). **h,** TSNE plots from sc-RNA seq of 2D iECs and iECs from 3D-oBRB.  
282 **i,** Gene expression differences between 2D iECs and iECs from 3D-oBRB for genes related to endothelial  
283 maturation, choroid, angiogenesis, and arterial development. Statistical significance was attributed to  
284 values of  $P < 0.05$  as determined by unpaired t-test. Data depicts results from n = 3012 cells (2D RPE), n =  
285 4380 cells (3D-oBRB RPE), n = 5369 cells (2D iECs), and n = 1294 cells (3D-OBRB iECs). \* $p < 0.05$ , All  
286 error bars indicate STE.

287

288

289

290

291

292

293

294

295

296

297

298

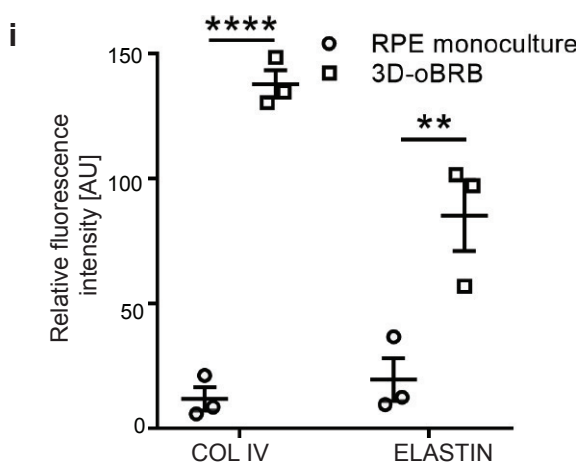
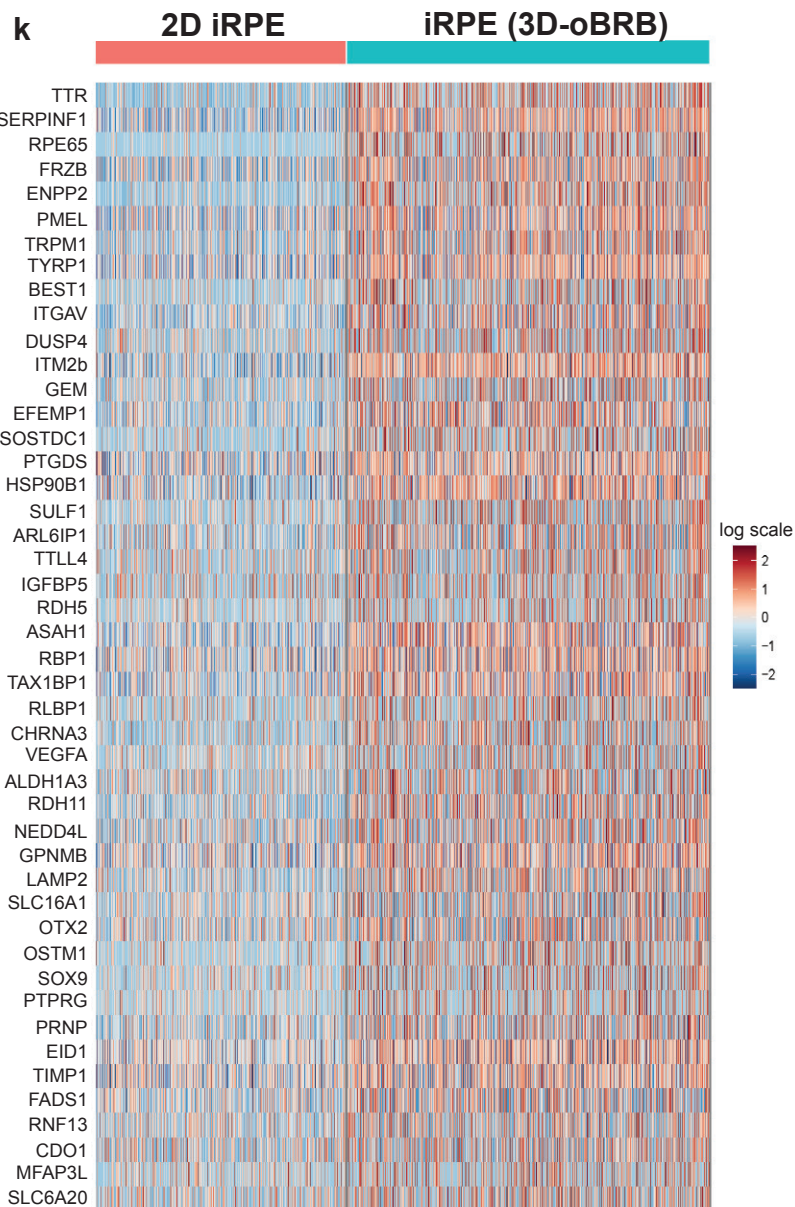
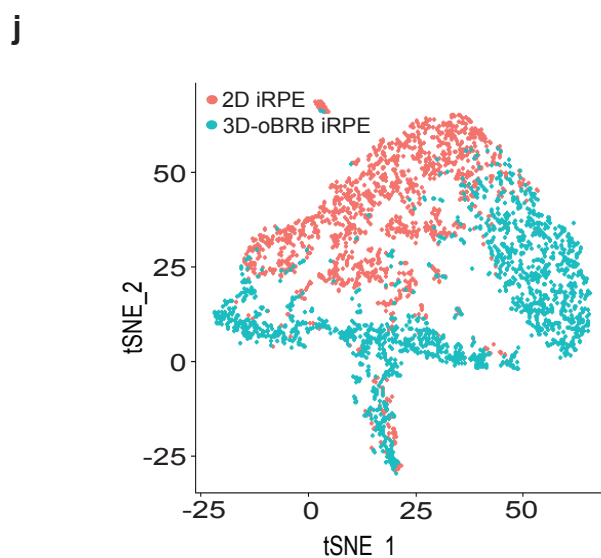
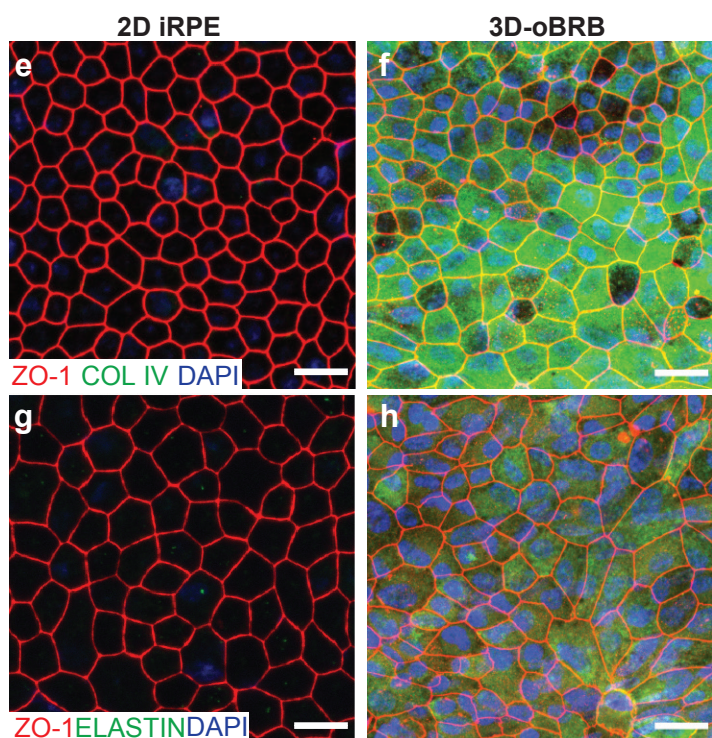
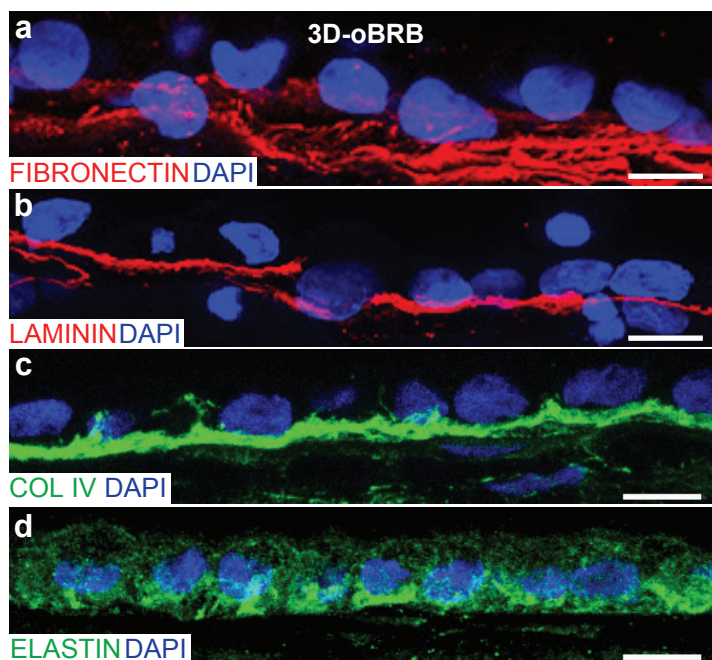
299 **Bruch's membrane formation in 3D-oBRB**

300 TEM suggested the formation of a Bruch's membrane-like structure between the RPE and the capillary-  
301 bed (Fig. 2b). We confirmed strong immunostaining for ECM components of native Bruch's membrane  
302 including FIBRONECTIN, LAMININ, COLLAGEN IV (COL IV), and ELASTIN<sup>16,24</sup> (Figs. 4a-d, movie  
303 S4). 3D rendering of ELASTIN and LAMININ immunostained images further revealed an acellular  
304 membranous zone underneath the RPE monolayer (movie S4). Quantification revealed a 15x higher COL  
305 IV expression and 4x higher ELASTIN expression in 3D-oBRB as compared to 2D-iRPE (Figs. 4 e-i). To  
306 determine the cellular origin of Bruch's membrane, we analyzed ECM-related gene expression in  
307 scRNAseq data. iRPE contributed to ECM proteins like *COL8A1* and *EFEMP1* - involved in Doyme  
308 honeycomb retinal dystrophy<sup>25</sup> whereas iECs were the major source of ECM proteins including *COL8A1*,  
309 *COL8A2*, *COL9A3*, *COL11A1*, *ELN* (Figs. S10a, b)<sup>26-28</sup>. All together this data shows that our 3D model  
310 enabled the creation of a Bruch's membrane-like structure *in vitro* that further enabled close interactions  
311 between RPE and choriocapillaris.

312 The presence of a Bruch's membrane-like structure prompted the question if iRPE grown on a natural ECM  
313 behave differently than iRPE grown on plastic substrates<sup>15</sup>. scRNAseq data confirmed this hypothesis. 46  
314 out of the previously reported 157 RPE signature-genes<sup>29</sup> were 1.5-4 log2 fold-higher in iRPE in the 3D-  
315 oBRB than 2D iRPE. Most notable were components of the visual cycle (*RPE65*, *RDH5*, *RBPI*, *RLBPI*,  
316 *RDH11*), angiogenic and non-angiogenic genes (*VEGFA*, *ENPP2* and *SERPINF1*), components of the  
317 Bruch's membrane (*EFEMP1*, *ITGAV*, *ITM2b* and *TIMP1*), and exosome assembly genes (*HSP90B1*,  
318 *LAMP2*, *SDCBP*) (Figs. 4j, k, S11a, b). Overall, this data provides additional evidence that as part of the  
319 3D-oBRB both iECs and iRPE attain more native-like properties including the formation of a Bruch's  
320 membrane equivalent structure.

321

322



323 **Fig. 4 | RPE maturity in 3D-oBRB. a-d**, Cross sections of 3D-oBRB immunostained for Bruch's  
324 membrane proteins FIBRONECTIN (a), LAMININ (b), COLLAGEN IV (COL IV) (c), and ELASTIN (d).  
325 Nuclei stained with DAPI. Scale bars, 10µm. **e-h**, 2D RPE monoculture (e, g) and 3D-oBRB (f, h), co-  
326 immunostained for COL IV (green) or ELASTIN with ZO-1 (red), and nuclei (blue). Scale bars, 30 µm. **i**,  
327 Fluorescence mean intensity comparison of ELASTIN and COL IV immunostaining in 2D-iRPE and 3D-  
328 oBRB models. (n=3). **j**, tSNE plots from sc-RNA seq of 2D-iRPE and RPE in 3D-oBRB. **k**, Gene  
329 expression of RPE signature genes, comparison between 2D-iRPE and RPE in 3D-oBRB. Statistical  
330 significance was attributed to values of  $p < 0.05$  as determined by two-way ANOVA and Sidak's multiple  
331 comparison test. \*\* $p < 0.01$ , \*\*\*\* $p < 0.0001$ . All error bars indicate STE.

332

333

334

335

336

337

338

339

340

341

342

343

344

### 345 **3D-oBRB recapitulates choroidal phenotypes seen in dry and wet AMD**

346 Drusen - a hallmark of dry AMD - accumulates under the RPE within the Bruch's membrane<sup>30</sup>. Complement  
347 competent human serum (CC-HS), has recently been linked to drusen formation<sup>31</sup>. Treatment of 3D-oBRB  
348 with 5% CC-HS induced APOE positive drusen-like deposits within the Bruch's membrane, as confirmed  
349 by histological analysis of 3D-oBRB in *en-face* view (APOE - purple, Figs. 5a,d), cross-sections (white  
350 lines, APOE - purple, Figs. 5g), and 3D rendered images (APOE - purple, movie S5). CC-HS treatment  
351 also led to RPE atrophy in 3D-oBRB (compare F-ACTIN – green Figs. 5b, e). Consistent with RPE atrophy,  
352 capillary degeneration was evident with CC-HS treatment (arrowheads; CD31 – red, Figs. 5c, f and g).  
353 Lastly, these structural changes in the 3D-oBRB led to a loss in its barrier resistance, as confirmed by a 20x  
354 drop in TER ( $p < 0.01$ ; Fig. 5h). Overall, these results validated 3D-oBRB as a physiologically relevant dry  
355 AMD model including subRPE drusen deposits, loss of barrier resistance, RPE atrophy, and capillary  
356 degeneration.

357

358 It is thought that hypoxia in the back of the eye leads to stabilization and nuclear translocation of the  
359 transcription factor HIF-1 $\alpha$  in the RPE<sup>32</sup>. HIF-1 $\alpha$  increases the expression and secretion of VEGF<sup>33</sup>, which  
360 leads to wet AMD. However, there is no direct proof to support this hypothesis for human ocular tissues.  
361 We sought to recreate wet AMD using RPE-specific hypoxia in the 3D-oBRB model. Treatment of the  
362 iRPE apical side with ML228 (2  $\mu$ M), a known HIF-1 $\alpha$  activator<sup>34</sup>, led to HIF-1 $\alpha$  activation in <5% of cells  
363 by 48 hours; by 96 hours elevated HIF-1 $\alpha$  protein levels was evident in 25% of cells (Figs. S12a, b, d, e).  
364 Continued treatment of ML228 for two weeks resulted in HIF-1 $\alpha$  activation in majority of iRPE cells and  
365 dropped iRPE monolayer TER close to zero; in comparison the TER of vehicle-treated cells wasn't changed  
366 (Figs. S12c, f, g). Consistently, HIF-1 $\alpha$  expressing cells also lost their epithelial phenotype, as confirmed  
367 by the loss of typical hexagonal morphology, unorganized ZO-1 expression, and an increase in cell size  
368 (Figs. S12e, f, and h).

369

370 Treatment of mature 3D-oBRB (on the apical side) with ML228 produced outcomes similar to seen in 2D-  
371 iRPE, including disruption of tight junctions and a 3-fold drop in tissue TER (Figs. 5i, j, o). Unlike 2D  
372 iRPE, in the 3D-oBRB model the TER did not drop to zero suggesting a protective effect of the capillary-  
373 bed on iRPE barrier resistance (Figs. S12g, 5o). Activation of HIF-1 $\alpha$  in the RPE of a mature 3D-oBRB  
374 initiated a CNV-like response with capillaries hyperproliferating towards the iRPE monolayer, as confirmed  
375 by image-based analysis of z-planes (Figs. 5k, l; yellow to red color of the code shows capillaries that are  
376 in the subRPE zone – white circles). Cross-sections of 3D rendered images of tissues clearly revealed  
377 capillaries hyperproliferating into the Bruch's membrane and expanding into the subRPE zone (Figs. 5 m,  
378 n - arrowheads; movie S6). To determine if the CNV-like response seen in our hypoxic 3D-oBRB model  
379 was VEGF induced, we measured VEGF secretion in ML228 treated 3D-OBRB. ML228 treatment led to  
380 a 5-fold increase in the apical VEGF secretion (Fig. 5p), while basal VEGF secretion did not change with  
381 ML228 treatment (Fig. 5q). Quantification of VEGF immunostaining revealed that most of the basally  
382 secreted VEGF accumulated around capillaries, likely binding to its cognate receptor - leading to CNV-like  
383 phenotype (Fig. 5r). Overall, the above data confirmed that our 3D-oBRB is able to recapitulate both dry  
384 and wet AMD phenotypes *in vitro*.

385

386

387

388

389

390

391



392 **Fig. 5 | RPE dependent choroid degeneration in dry and wet AMD models of 3D-oBRB. a-g, *En face***  
393 **(a-f), cross-section (g) views of APOE (magenta), CD31 (red) immunostaining, F-ACTIN (green), Hoechst**  
394 **(blue) in complement competent human serum (CC-HS) treated and control 3D-oBRB. Arrowheads mark**  
395 **degenerated RPE and capillaries. Scale bars, 100 $\mu$ m. (g) white vertical lines mark Bruch's membrane. Scale**  
396 **bars, 10 $\mu$ m. (n=3) h, TER of control and CC-HS treated 3D-oBRB (n=3). i,j, Confocal images of RPE from**  
397 **3D-oBRB, immunostained with ZO-1 (green) and Hoechst (blue). Arrowhead marks lost ZO-1 signal. Scale**  
398 **bars, 30  $\mu$ m. k,l, Depth code of 3D reconstructed confocal images. Color gradient along z-axis (100  $\mu$ m**  
399 **depth) starting from subRPE zone (red) to the end of choroid (blue); in vehicle-treated 3D-oBRB (k) and**  
400 **in ML228 treated 3D-oBRB (l). Arrowheads mark capillaries in the sub-RPE region. Scale bars, 100  $\mu$ m.**  
401 **m,n, Side view images of CNV, immunostained with ZO-1 (green) and CD31(red). Scale in x-axis, 50 $\mu$ m**  
402 **and in z-axis, 10 $\mu$ m. i-n, (n=5) o, TER measurement on vehicle or ML228 treated 3D-oBRB (n=5). p, q**  
403 **apical (p) and basal (q) VEGF secretion in vehicle and ML228 treated 3D-oBRB (n=4). r, Fluorescence**  
404 **intensity of VEGF staining in cryosectioned 3D-oBRB tissue slice. Quantification of subRPE region (0.0**  
405 **fractional distance) to the bottom of the choroid layer (1.0 fractional distance) (n=3). Statistical significance**  
406 **was attributed to values of  $p < 0.05$  as determined by paired t-test (o,p,q) or two-way ANOVA and Sidak's**  
407 **multiple comparison test (g,h). \* $p < 0.05$ , \*\*\* $p < 0.001$ , \*\*\*\* $p < 0.0001$ . All error bars indicate STE**  
408 **(g,o,p,q,r).**

409

410

411

412

413

414

## 415 **Bevacizumab halts CNV in the 3D-oBRB disease model**

416 To validate our CNV model for drug discovery, we asked whether we could replicate the efficacy of an  
417 anti-VEGF monoclonal antibody (bevacizumab), used for the treatment of wet AMD<sup>6</sup>. We co-treated 2D  
418 iRPE and 3D-oBRBs with ML228 and a clinical dose (0.3 mg/mL) of bevacizumab. Bevacizumab had little,  
419 if any, effect reversing ML228-induced 2D iRPE atrophy (Figs. 6a-d). In contrast, in the 3D-oBRB  
420 bevacizumab co-treatment with ML228 partially recovered RPE epithelial phenotype as confirmed by  
421 regained epithelial morphology in ZO-1 immunostained images (arrowheads, Figs. 6e-g) and doubled TER  
422 values of ML228+ bevacizumab co-treated tissues (Fig. 6d). 3D reconstruction of tissue cross-sections  
423 revealed a noticeable reduction in CNV with bevacizumab and ML228 co-treatment as compared to ML228  
424 treatment alone (arrowhead, Figs. 6h-j, movie S6). Image-based quantification of vascular density in each  
425 focal plane showed a 3-fold higher ( $p < 0.05$ ) capillary density within 5 $\mu$ m of the iRPE monolayer in ML228  
426 treated samples that were suppressed entirely in bevacizumab and ML228 co-treated samples (Fig. 6k).  
427 There was no significant difference in vascular density deeper than 10 microns in the tissue (Figs. 6k, S13a-  
428 c). Overall, these results suggest that hypoxia induced CNV seen in our 3D-oBRB is primarily VEGF  
429 induced and can be suppressed by the clinically used drug bevacizumab. All together, these results validate  
430 the utility of our tissue for discovering new drugs to treat AMD.

431

432

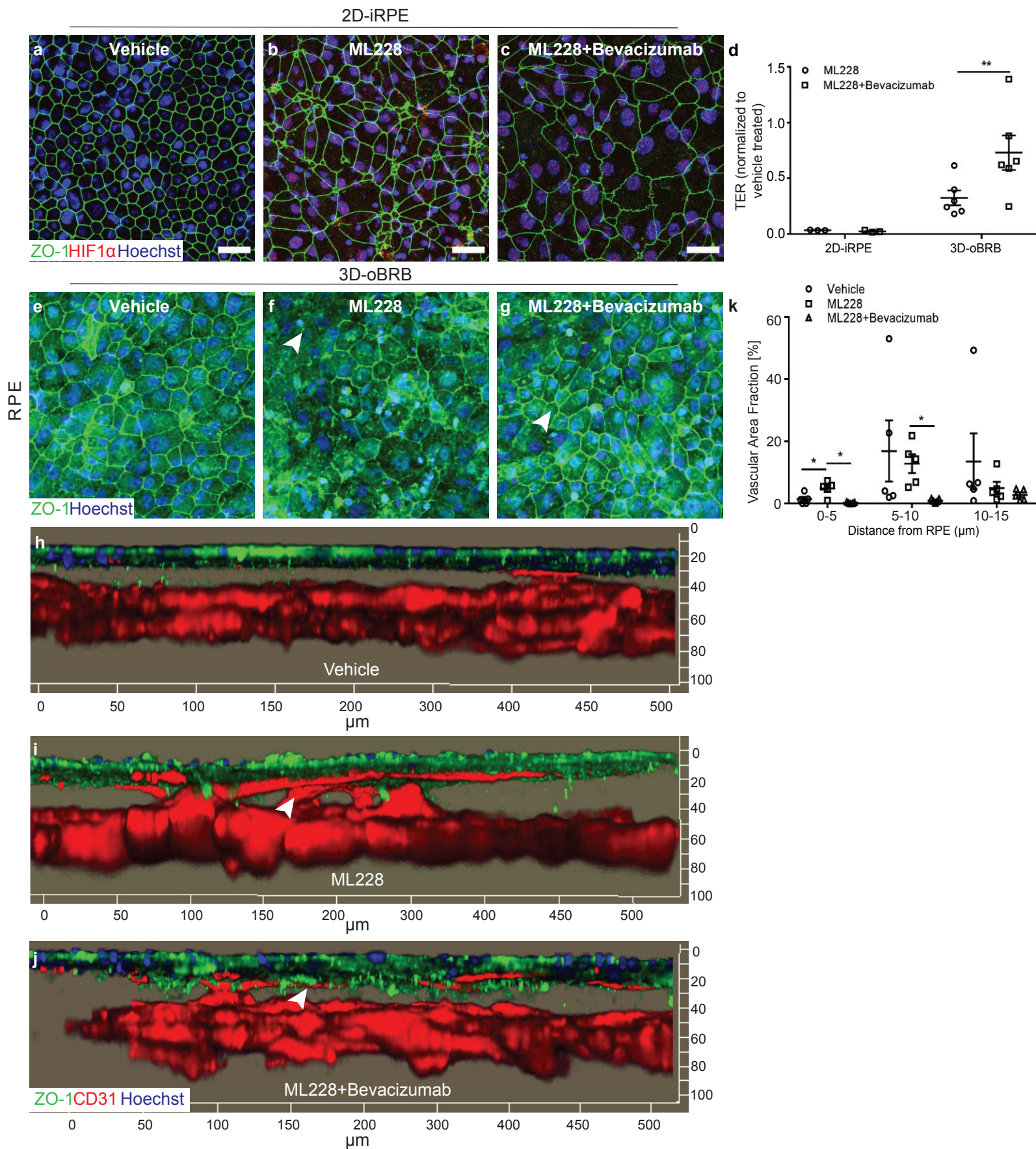
433

434

435

436

437



438 **Fig. 6 | Bevacizumab treatment suppresses wet-AMD in 3D-oBRB. a-c,** RPE monoculture at 2 weeks  
439 treated with DMSO as a vehicle control **(a)**, ML228 (2 $\mu$ M) **(b)**, and ML228 (2 $\mu$ M)+bevacizumab  
440 (0.284mg/ml) **(c)**, immunostained for HIF-1 $\alpha$  (red), ZO-1 (green), and nuclei stained with Hoechst (blue).  
441 Scale bars, 30 $\mu$ m. (n=3). **d,** TER measurement comparison between 2D-iRPE and 3D-oBRB for ML228  
442 and ML228+bevacizumab treated samples. TER values were normalized to vehicle treated 3D-oBRBs.  
443 (2D-iRPE, n=3; 3D-oBRB, n=6). **e-g,** Maximum intensity projection images of RPE of 3D-oBRB,  
444 immunostained with ZO-1 (green) and stained with Hoechst for nuclei (blue). Degenerated and recovered  
445 RPE are marked with arrowheads in **(f and g)**. Scale bars, 25 $\mu$ m. **h-j,** Side view of 3D reconstructed images  
446 of vehicle **(h)**, ML228 **(i)**, and ML228+bevacizumab **(j)** treated 3D-oBRB tissues, immunostained with  
447 ZO-1 (green) and CD31(red). Arrowheads in **(i)** mark hyperproliferating capillaries and in **(j)** mark retracted  
448 capillaries. Scale in x-axis, 50 $\mu$ m and in z-axis, 10 $\mu$ m. **e-j,** (n=4). **k,** Vascular area fraction was calculated  
449 from CD31 positive area in each z-stack. (n=5). Statistical significance was attributed to values of  $p < 0.05$   
450 as determined by unpaired t-test (m) or two-way ANOVA and Sidak's multiple comparison test **(d,h,l)**.  
451 \* $p < 0.05$ , \*\* $p < 0.01$ , \*\*\*\* $p < 0.0001$ . All error bars indicate STE.

452

453

454

455

456

457

458

459

460

## 461 Discussion

462 3D-oBRB recapitulated key native features that have not been previously replicated *in vitro*: **(1)** a fully  
463 mature and polarized RPE monolayer with basal infoldings that are critical for metabolite transport and  
464 membrane trafficking. Consistently, an increased expression of exosome transport genes was seen in iRPE  
465 in the 3D-oBRB. Basal infoldings are lost in diseases like choroideremia and AMD, underscoring the  
466 importance of our 3D-oBRB for studying both monogenic and polygenic eye diseases<sup>35</sup>; **(2)** a Bruch's  
467 membrane that mediates RPE and capillary interactions. Its hydraulic conductivity ensures the free flow of  
468 nutrients, metabolites and cytokines between the two tissues<sup>28</sup>. With age and in AMD, loss of Bruch's  
469 membrane hydraulic conductivity disrupts communication between the two tissues and is thought to be the  
470 cause of outer retina degeneration<sup>36</sup>. Our 3D-oBRB replicates degenerative changes in the Bruch's  
471 membrane (APOE deposits and angiogenic invasion) and allows the possibility of discovering how such  
472 changes contribute to disease; and **(3)** a capillary-bed with a functional lumen, fenestration, choroid-specific  
473 gene expression and ability to integrate upon transplantation. Loss of fenestration is associated with AMD  
474 risk-alleles and advanced AMD<sup>18</sup>. Our model provides direct evidence that fenestration is dependent on the  
475 presence of healthy RPE and a possibility of understanding the role of AMD risk-alleles via the use of  
476 patient iPSCs.

477

478 These features were possible due to the introduction of several innovative bioengineering attributes: **(1)** a  
479 biodegradable scaffold provided two bioactive surfaces allowing RPE monolayer growth on one side and  
480 bioink printing on the opposite side. Scaffold micropores allowed RPE and ECs to deposit ECM leading to  
481 the formation of a Bruch's membrane to recreate a native-like tissue architecture<sup>2</sup>; **(2)** the mixture of gelatin  
482 and fibrin provided a temperature-sensitive hydrogel with high fluidity at room temperature for developing  
483 a homogenously concentrated bioink of ECs, pericytes, and fibroblasts and low fluidity at 10°C for  
484 relatively easier bioprinting. Fibrin maintained the 3D tissue structure until fibroblasts secreted sufficient  
485 ECM to provide substrate for a stable capillary-bed; **(3)** a combination of relevant cell types at appropriate

486 ratio: 2:1 fibroblasts to ECs and 1:10 pericytes to ECs allowed easier EC migration and angiogenesis  
487 through a native-like ECM structure and sustained long-term capillaries of the correct lumen size (5-20µm).  
488 RPE cells provided VEGF for capillary growth, confluency, fenestration, and choroidal phenotype.

489

490 Our 3D-oBRB constructs recapitulated AMD phenotypes and shed light on disease mechanisms that could  
491 not be addressed previously due to the lack of appropriate *in vitro* model systems. In 3D-oBRB, drusen  
492 accumulated within the Bruch's membrane, similar to the observation in AMD eyes<sup>2,3</sup>. This allowed  
493 monitoring of drusen impact on Bruch's membrane. RPE atrophy led to choroid degeneration, providing a  
494 direct proof of observations made in AMD cadaver eyes that suggested RPE atrophy precedes choroid  
495 degeneration. The data from our model suggests that complement inhibition might be a potential therapeutic  
496 strategy at an earlier disease stage before the RPE atrophy begins. Our model also provides direct proof  
497 supporting previous work that suggested CNV is induced by abnormal VEGF secretion by RPE cells<sup>37,38</sup>.  
498 We provide additional insight into CNV by showing higher VEGF secretion induced by RPE hypoxia; and  
499 binding of basally secreted VEGF to ECs – combined these data suggest a combination of HIF-1α inhibitor  
500 with a VEGF-receptor blocker will be a more effective in CNV, especially where anti-VEGF agents have  
501 failed.

502

503 Here we have developed a relatively complete model of the oBRB and validated its clinical relevance by  
504 demonstrating the efficacy of a clinically used anti-VEGF antibody. A fully-syngeneic 3D-oBRB derived  
505 from AMD-patient iPSCs will help provide a more comprehensive understanding of disease pathology and  
506 help determine the role of genetics in disease manifestation.

507

508 **Methods**

509 **Donor tissues**

510 Human cadaver eyes were obtained from the Advancing Sight Network (Alabama Eye Bank, Birmingham,  
511 AL). Use of cadaver eyes was exempt from the NIH Institutional Review Board approval.

512 **Tissue culture media**

513 RPE Maintenance Media (RPE-MM) components includes basal MEM alpha-modified media (Sigma-  
514 Aldrich, Cat# M-4526, St. Louis, MO) supplemented with N-2 supplement (1% v/v, Gibco, Cat# 17502048,  
515 Waltham, MA), Glutamine, Penicillin and Streptomycin (1% v/v, Sigma-Aldrich, Cat# G1146), Non-  
516 essential Amino Acids (5mL, Sigma-Aldrich, Cat# M7145), a Taurine, Hydrocortisone and Triiodo-  
517 Thyronin cocktail dissolved in DPBS (125 mg/10 ug/0.0065 ug, Sigma-Aldrich, Cat# T-0625/H-0396/T-  
518 5516) and heat-inactivated fetal bovine serum (5% v/v, FBS, Sigma-Aldrich, Cat# F4135-6X500ML/6505).  
519 iPSC Endothelial Cell Media (iCell Media) consists of VascuLife Basal Medium (Thermo Fisher Scientific,  
520 Cat# LL-0003, Waltham, MA), growth factors from the VEGF LifeFactors® Supplement Kit (LifeLine  
521 Cell Technologies, Cat# LS-1020, Frederick, MD), and iCell Endothelial Cells Medium Supplement  
522 (Cellular Dynamics International, Cat# M1019, Madison, WI). Note that fetal bovine serum and gentamycin  
523 were excluded from the LifeFactors® supplement kit. All Media was filtered through sterile 0.22 µm pore  
524 filters before use.

525 **Cell/Tissue Culture**

526 Human placental microvascular pericytes (Angio-Proteomie, Cat# cAP-0029, Boston, MA) were cultured  
527 on 25 cm<sup>2</sup> Easy Flasks (Thermo Fisher Scientific, Cat# 156367) coated with quick coat solution (3mL,  
528 Angio-Proteomie, Cat# cAP-01). Pericytes were cultured in RPE-MM, which is changed every other day.  
529 Pericytes were passaged up to three times prior to 3D bioprinting. iCell endothelial cells (Cellular Dynamics  
530 International, Cat# R1022) were cultured on 75 cm<sup>2</sup> Easy Flasks (Thermo Fisher Scientific, Cat# 156499)  
531 coated with Fibronectin (Gibco, Cat# 33016-015). The cells were cultured in the iCell Media with media  
532 changes occurring every other day. Cells were passaged at > 70% confluence by incubating cells in

533 0.25%Trypsin-EDTA (1X, Gibco, Cat#.25200-056) for 5 minutes at 37°C. The cells were then resuspended  
534 in iCell complete endothelial medium and centrifuged at 200 RCF for 5 minutes. The cells were passaged  
535 up to two times prior to 3D Bioprinting. The adult choroidal fibroblasts were isolated from cadaver human  
536 eyes which were procured from Alabama Eye Bank. Fibroblasts were cultured on Primaria tissue culture  
537 flasks (Corning, Cat# 353824, Corning, NY) in RPE-MM.

538 iPSC derived Retinal Pigment Epithelium (iPSC-RPE) were purchased from Cellular Dynamics  
539 International. iPSC-RPE cells were seeded with initial density of  $2.5 \times 10^5$  cells/well on a vitronectin coated  
540 transwell membrane (0.5 mg/mL, Thermo Fisher, Cat# A31804; Corning, Cat# 3407). The medium was  
541 changed every other day. After two weeks of post-seeding, RPE maintenance media supplemented with  
542 Prostaglandin E2 (Tocris Biosciences, Cat# 363-24-6, Bristol, United Kingdom) at a 100  $\mu$ M concentration  
543 were fed to the iPSC-RPE cells for maturation.

#### 544 **Biodegradable scaffold and bioink**

545 Scaffolds used to support 3D-oBRB were constructed by modifying commercially available trans-well  
546 inserts (Corning, Cat# 3407). The permeable membranes included with the inserts were removed and  
547 replaced with 12-mm diameter circular sheets of biodegradable PDLGA scaffold (Polysciences, Cat#  
548 052218-6\_1\_20\_20\_55\_24, Warrington, PA; Biosurfaces, Boston, MA). Following the removal of the  
549 transwell membranes, the transwell frames were dipped into Kwik-Cast silicone gel (World Precision  
550 Instruments, Cat# KWIK-CAST, Sarasota, FL), and the PDLGA scaffolds were attached to the frames. The  
551 gel solidified for 5 minutes with the scaffold facing up. Afterward, O-rings (Inner diameter: 10.4mm, Outer  
552 diameter: 14.5mm), which were 3-D printed using an Ultimaker2+ 3D Printer (Ultimaker, Utrecht,  
553 Netherlands), were treated on its inner surface using additional Kwik-Cast gel and attached to the basal side  
554 of the modified transwells. The gel solidified for 10 minutes, permanently attaching the scaffolds to the  
555 transwell frame. The scaffolds were coated on the apical side with vitronectin and incubated for an hour at  
556 room temperature, followed by an additional hour of incubation at 37°C. Afterward, vitronectin from the  
557 apical side was aspirated and 4 mL of cell culture grade water was added to the bottom of the scaffold in

558 well plates. The scaffolds were then incubated at 37°C for 2 hours. Following incubation, the water was  
559 aspirated, and the scaffolds were dried overnight.

560 On the day of bioprinting, a 2.5 mg/mL fibrinogen solution (Sigma-Aldrich, Cat# F3879, St. Louis, MO)  
561 was prepared in DPBS (Calcium and Magnesium free, Thermo Fisher Scientific, Cat# 14190144, Waltham,  
562 MA) to encapsulate cells during “choroid” printing. Aprotinin (0.075 U/mL, Sigma, Cat# A4529) was  
563 added to the fibrinogen solution, and the entire solution was filtered through a sterile 0.22 µm filter.  
564 Following filtration, a 300 mg sample of Novogel 2.0 (Organovo 3D Bioprinting Solutions, Cat# NVG-2.0,  
565 San Diego, CA) was carefully added to 5 mL of the fibrinogen solution. The solution was incubated in a  
566 37°C water bath to dissolve the Novogel powder. After dissolution, the completed 2.5 mg/mL fibrinogen  
567 solution was incubated at 37°C for 1 to 2 hours prior to cell encapsulation. A 5.0 mg/mL fibrinogen solution  
568 was prepared identically to the 2.5 mg/mL solution above without the addition of Novogel powder. This  
569 solution was placed at 4°C until bioprinting.

#### 570 **Bioprinting of “choroid” and 3D-oBRB maturation**

571 Following assembly of the scaffolds and immediately before bioprinting, the scaffolds were treated in a  
572 Plasma Etch PE-50 oxygen-plasma etcher at maximum power (150W, Plasma Etch, Inc., Carson City, NV)  
573 for 30 minutes under 10 CC/min O<sup>2</sup> flow to sterilize and improve surface hydrophilicity.

574 Fibroblasts, endothelial cells, and pericytes were trypsinized from cell culture flasks as described previously.  
575 Cells were encapsulated at the following densities in the 2.5 mg/mL fibrinogen solution: 1.0 to 1.2 x 10<sup>7</sup>  
576 Fibroblasts/mL; 5.0 to 7.0 x 10<sup>6</sup> Endothelial cells/mL; and 5.0 to 7.0 x 10<sup>5</sup> Pericytes/mL. The three cell  
577 types were combined and centrifuged at 500 RCF for 4 minutes before resuspension in the 2.5 mg/mL  
578 fibrinogen solution. Resuspension and mixing were conducted using a sterile spatula (Corning, Cat# 3004)  
579 to prevent air bubble formation in the suspension. The cell suspension transferred to a sterile Hamilton  
580 Gastight syringe without air bubbles (Hamilton, Cat# 1750). The syringe was then sealed and placed at 4°C

581 for 12-15 minutes with the dispensing side facing up. A NovoGen MMX Bioprinter™ (Organovo, San  
582 Diego, CA) was used to extrude the solution onto the biodegradable polymer scaffolds.

583 After the structure was printed, 360 µL of 5 mg/mL fibrinogen solution was added to a 40 uL aliquot of 10  
584 U/mL thrombin. 170 uL of the 5 mg/mL fibrin gel with thrombin was then added directly to the printed  
585 structure to form a supporting fibrin gel structure between printing lanes. It solidified for 15-20 minutes.  
586 Printing Medium, which consists of a 1:2 ratio of iCell media and serum-free RPE-MM that was  
587 supplemented with 1.67% heat-inactivated FBS, thrombin (0.5 U/mL, Sigma, Cat# T6884), rh ANG-1  
588 (100ng/mL, R&D Systems, Cat# 923-AN, Minneapolis, MN), VEGF (85 ng/mL, R&D systems, Cat# 293-  
589 VE-500), and aprotinin, was then added to the well (0.5 mL apically, and 3.5 mL basally) and placed at  
590 room temperature 2 hours. The samples were then placed in a 37°C, 5% CO<sub>2</sub> incubator overnight.

591 Bioprinted 3D-oBRB tissues consist of multiple cell types such as endothelial cells, pericytes, fibroblasts,  
592 and iPSC-RPE and were incubated under a complex medium changing schedule (Table 1). RPE cells were  
593 seeded on the apical side of the PDLGA scaffold at day 7 after bioprinting.  $2.5 \times 10^5$  RPE cells were added  
594 to each bioprinted tissue in suspension of RPE-MM. The RPE growth and maintenance media were used  
595 according to table S1. Printing Media was applied to the apical and basal sides of the tissue on the day of  
596 the print. Tissues were then fed on the apical and basal sides using Vascular Development Media  
597 (VDM), which has the same composition as Printing Media but with thrombin removed, from day 2 to day  
598 7. On day 7, the apical sides of the tissues were fed using 5% RPE, while the basal sides of the tissues were  
599 fed using Vascular Growth Media with Aprotinin (VGM+AP), which excludes ANG-1 and VEGF from  
600 VDM. On day 14, the apical sides of the tissues continued to be fed using 5% RPE, while basal sides of the  
601 tissues were fed using VGM which excludes Aprotinin from VGM+AP. On day 21, media conditions were  
602 identical to the previous week, except that the 5% RPE medium was supplemented with Prostaglandin E2  
603 at a 100 µM concentration on the apical side. From Day 29 onward, media conditions were identical to the  
604 previous week, except that Vascular maintenance media (VMM), which excludes VEGF completely,  
605 replaced VGM medium on the basal side.

## 606 **Rat Transplantation**

607 The tissue was gently wash with BSS+ (Alcon Inc, Cat# 00065079515) and a thin layer of Healon PRO  
608 (Johnson & Johnson Vision Care Inc) was used to protect it during manipulation. A 1.5mm (Acuderm Inc  
609 Cat# P1525) puncher was used to cut the dose to deliver from the cultured tissue. RNU rats from Charles  
610 River Laboratories, Inc., Wilmington, MA were used in this study. The animals (n=4, males, between 250  
611 and 300 g) were anesthetized with IP injection of Ketamine (65 mg/kg, VetONE Inc, Cat#13985-702-10)  
612 and 7.5 mg/kg Xylazine (7.5 mg/kg, Akorn Inc, 59399-111-50). Animals were then placed on a shaped  
613 foam holder and the body was covered to avoid body temperature drop. Isoflurane was administered in  
614 mask, 1% with an oxygen flow rate of 300 ml/min, to maintain anesthesia. Eyes were exposed and secured  
615 by a suture tide around the eyeball (Figure X). Proparacaine (0.5%, Novartis, Cat# 61314-016-01) was used  
616 as local anesthetic and the pupil were dilated with Phenylephrine (Paragon Biotek, 4270210215) and  
617 Tropicamide (Novartis, Cat# T2018-39) eye drops. GenTeal lubricant eye gel (Alcon, Cat# US-GNT-VLC-  
618 2000008) and a glass cover slip were used as a lens substitute to visually access the back of the eye. A  
619 2.2mm knife was used for sclerotomy, vitreous was replaced with 2% Hyaluronic acid (HA) (Sigma Aldrich,  
620 Cat# H7630) and the retina was detached with 0.5% HA (Figure X). The tissue was then delivered in the  
621 subretinal space with end-grasping ophthalmic forceps (Figure X). The retina was flattened with 2% HA.  
622 The suture used to expose the eye was removed and topic Neo-Poly-Bac (Bausch & Lomb, Cat#  
623 *IWM044525*) ophthalmic ointment was used to prevent infections. Animals were kept in a warm, dark and  
624 quiet environment until complete recover from anesthesia, then were single caged until the end of the  
625 experiment. Two weeks after surgery animals were euthanized by CO<sub>2</sub> overdose and perfused with 1,1'-  
626 dioctadecyl-3,3,3',3'-tetramethylindocarbocyanine perchlorate (DiI) (Sigma Aldrich, Cat# 42364) a  
627 lipophilic carbocyanine dye, which incorporates into endothelial cell membranes upon contact (Li et al.,  
628 2008). The dye was prepared and administered as previously described by Li, followed by 4% PFA  
629 perfusion. Eyes were collected and fixed in 4% PFA overnight.

## 630 **Modeling Wet and Dry AMD**

631 We modeled wet and dry AMD on four-week-old tissue using a chemical stressor or complement competent  
632 human serum, respectively. For Wet-AMD, ML228 (2  $\mu$ M) was introduced to the apical side of RPE and  
633 treated for four days, and Bevacizumab (0.284 mg/mL, NIH clinical center) was treated with ML228 after  
634 the four days of the ML228 treatment. ML228 was treated every day and Bevacizumab was treated every  
635 other day. For Dry AMD, complement competent human serum (5%) was treated to both apical and basal  
636 side of the tissue with everyday media change. The total inducing period for both AMD models is two  
637 weeks.

### 638 **Trans-Epithelial Resistance measurements and fixation**

639 The junctional integrity of 3D-oBRB tissues or iPSC-RPE monolayers were examined prior to fixation.  
640 Trans-Epithelial Resistance (TER) was measured using an EVOM2 Epithelial Volt/ohm meter (World  
641 Precision Instruments, Cat# 300523) and an Endohm-245NAP well container (World Precision  
642 Instruments). Afterward, tissue samples were incubated in 4% Paraformaldehyde in 1x PBS at 4°C  
643 overnight for fixation and were washed three times for 10 minutes in 1x PBS. At this point, whole tissue  
644 samples were either Cryosectioned (See: Cryosectioning) or Paraffin-sectioned (See: Paraffin-sectioning)  
645 or immunostained (See: Immunostaining). If whole tissue samples were to be immunostained directly,  
646 samples were permeabilized using in 0.5% Triton X-100 (Thermo Fisher Scientific, Cat# 85112) solution  
647 in 1x PBS. Samples were punched out using a biopsy punch, transferred to the 24 well and blocked in 5%  
648 goat serum, 0.1 % Triton X-100 and 1%BSA in 1x PBS for 1 hour at room temperature. Afterward, the  
649 samples were washed three times for 10 minutes in 1x PBS.

650

651

### 652 **Microscopy**

653 Time lapse images of GFP labeled endothelial cells were taken by aEVOS Auto FL (Thermo Fisher  
654 Scientific, NY). Time-course immunofluorescent images for quantification were taken by using Leica TCS-

655 SP8 (Leica, Wetzlar, Germany) and Zeiss LSM710 (Zeiss, Oberkochen, Germany) confocal microscopes.  
656 3D reconstructed images with high magnification (x25) were taken by SP8 confocal microscope (Leica).  
657 Transmission electron microscopy with glutaraldehyde fixed samples was taken by the NEI core facility  
658 using a JEM-1010 electron microscope (JEOL, Peabody, MA).

659

## 660 **Histology and immunofluorescence**

661 **Cryosectioning:** Fixed tissue samples were punched from transwell inserts using a 10-mm biopsy punch  
662 and incubated in 15% sucrose, followed by 30% sucrose until the water was sufficiently removed from the  
663 tissue sample (approximately 1-hour incubation per solution). Rat Ocular Tissue was extracted from  
664 animals, and then flash frozen. Afterward, the tissues were embedded in Optical Cutting Temperature  
665 Embedding Medium (Thermo Fisher Scientific, Cat# 23-730-571) and frozen using dry ice for a minimum  
666 of 90 minutes. The samples were stored in -80°C until sectioning. The tissues were cut to to 12- $\mu$ m-  
667 thickness slices and loaded onto glass slides using a cryostat (Leica, Germany) at -30°C cutting temperature  
668 and -15°C sample head temperature. Prior to staining, tissue slices were heated on a hot plate to 37°C for  
669 30 minutes to secure the section to the glass slide. The tissues were then either H&E stained using an  
670 automated H&E Staining machine (Bond RX; Leica, Germany), or immunostained. During  
671 immunostaining, the slices were blocked and permeabilized using 0.5% Triton X-100 (Thermo Fisher  
672 Scientific, Cat# 85112) prior to the application of primary and secondary antibodies.

673 **Paraffin Sectioning:** Fixed samples were permeabilized for 30 minutes in 0.5% Triton X-100 (Thermo  
674 Fisher Scientific, Cat# 85112). After permeabilization, samples were punched out from transwell inserts  
675 using a 10-mm biopsy punch and stored in 24-well plates. Samples were then blocked in 5% goat serum,  
676 0.1 % Triton X-100 and 1%BSA in 1x PBS for 1 hour at room temperature. Afterward, the samples were  
677 washed three times for 10 minutes in 1x PBS.

678 **Vibratome Sectioning:** Fixed 3D-oBRB and Rat Ocular tissues were embedded in 6.8% w/v Type 7-A  
679 Agarose (Sigma-Aldrich, Cat# A0701) and cut into 100 µm sections on the Leica VT 1200S vibratome  
680 (Leica, Wetzlar, Germany). Sectioned samples were blocked, permeabilized, and washed prior to staining  
681 as described previously

682 **Immunostaining:** Primary antibodies were diluted in 1X PBS containing 0.1% Triton-X-100 and 1% BSA  
683 and 3D-oBRB tissues, or iPSC-RPE monolayers were incubated at 4°C overnight. Primary antibodies  
684 included Mouse anti-PLVAP (FELS, 1:50, Abcam, Cat# AB81719); Rabbit anti-CD31 (1:50, Abcam, Cat#  
685 AB28364); Mouse anti CD31 (1:50, Agilent, Cat# M0823); Rabbit anti-Laminin (1:50; Abcam, Cat#  
686 AB11575); Mouse anti E-cadherin (1:100; Abcam; Cat# AB40772); mouse anti-ZO-1 (1:100; Thermo  
687 Fisher Scientific, Cat# 33-9100); rabbit anti-ZO-1 (1:50; Thermo Fisher Scientific, Cat# 61-7300) Mouse  
688 anti-Collagen-IV (1:50; Abcam, Cat# AB6311); Rabbit anti-Elastin (1:50 Abcam, Cat# AB21610); Rabbit  
689 anti-APOE (1:50; Abcam, Cat# AB52607), Rabbit anti-VEGF (1:50; Thermo Fisher Scientific, Cat# P807),  
690 Mouse anti-STEM121 (1:100; Takara Bio, Cat# Y40410), Rabbit anti-VWF (1:100; Dako, Cat#GA52761-  
691 2) and Alexa-Fluor™ 647-Phalloidin (26 nM, Thermo Fisher Scientific, Cat# A22287). Blocking controls  
692 were performed using primary antibody buffers without the use of primary antibodies. Samples were then  
693 washed three times for 10 minutes in 1x PBS. Secondary antibodies were diluted (PBS containing 0.1%  
694 Triton-X-100 and 1% BSA). Secondary antibodies included Alexa-fluor™ Goat anti Rabbit 647 (Invitrogen,  
695 Cat# A21244); Goat anti Rabbit 594 (Life Technologies, Cat# A11012); Goat anti Rabbit 555 (Invitrogen,  
696 Cat# A32732); Goat anti-Rabbit 488 (Invitrogen, Cat# A11008); Goat anti-mouse 647 (Invitrogen, Cat#  
697 A32728); Goat anti-mouse 595 (Invitrogen, Cat# A11032); Goat anti-mouse 555 (Invitrogen, Cat# A21422);  
698 Goat anti Mouse 488 (Invitrogen, Cat# A32723). Secondary antibodies were incubated with Hoescht 33342  
699 nuclear stain (1:2000) in the dark at room temperature for 4 hours. Samples were washed 3 times for 10  
700 minutes in 1xPBS. Cryosectioned, Parafilm-sectioned and whole tissue samples were mounted using  
701 Fluoromount G (Southern Biotech, Cat# 0100-01, Birmingham, AL) following immunostaining.

702

703 **Quantification**

704 **Angiogenesis quantification:** Fluorescent images of vasculature at 4, 6, and 8 days after bioprinting, either  
705 non-treated or treated with varying doses of VEGF were quantified using MATLAB version 2019b  
706 (Mathworks, Natick, MA). Six line probes, numbered 1 to 6, were created in the acellular spaces between  
707 printed stripes. Fluorescence intensity peaks with a threshold (100 in 8-bit gray scale) that overlapped with  
708 the line probes were quantified in each image (Fig. S2). The counted peaks from each line number were  
709 averaged per each vascular micrograph, representing the “edges” to “centers” of the acellular space. To  
710 determine the directionality and persistence of blood vessel migration into the acellular regions, an  
711 angiogenesis index was created to quantify mean blood vessel length perpendicular to the printed stripes.  
712 Confocal images were processed as maximum intensity projection images and the angiogenesis index was  
713 measured using MATLAB (Mathworks). Briefly, regions of interest were defined in acellular spaces as a  
714 space within 250 pixels of a line probe generated through the center of the spaces. Acellular spaces that  
715 overlapped with out-of-focus endothelial cell clusters were excluded from analysis (Fig. S5b). Blood  
716 vessels were defined as objects that were greater than 20 pixels in length and expanded to within a mean  
717 distance of 85 pixels of the line probe. Angiogenesis index was calculated using maximum ferret angle of  
718 each blood vessel relative to the line probe and maximum ferret diameter of each blood vessel [equation  
719 (1)].

720 
$$(1) Index = | \sin (MaxFerretAngle) * MaxFerretDiameter |$$

721 **FELS immunostaining quantification for the analysis of vascular network in 3D-oBRB tissues:**

722 Immunostaining images of CD31 and FELS were analyzed using ImageJ to quantify the vascular networks  
723 in 3D-oBRB tissues. Any CD31-labeled images taken one week after bioprinting were contrasted with  
724 isolating the brightest 80% of pixels (Leica TCS-SP8 and Zeiss LSM710) from the background. For the  
725 rest of the time points, CD31-labelled images were contrasted with isolating the brightest 20% of pixels  
726 from the background. FELS-labeled images were contrasted with separating the brightest 5% of pixels from  
727 the background at all time points. The area ratios were taken between FELS-positive area/image and the

728 combined area of CD31 and FELS-positive signal to quantify the area of CD31 that was co-occupied by  
729 FELS.

730 **VEGF Immunostaining Quantification:** Z-stacks of the VEGF-A-stained cryosectioned tissue slices were  
731 analyzed using ImageJ. The images were converted into maximum intensity projection images before  
732 quantification. For image quantification, a Gaussian Blur Filter (radius 4.0 px) was applied to reduce noise  
733 in the images. The average pixel brightness along the thickness of the slice was quantified for each slice to  
734 identify areas of high VEGF concentration in the slices. Phalloidin 647 staining was used to identify the  
735 apical (RPE) and basal (choroid) ends of the tissue slices.

736 **Cytokine Quantification:** To quantify the cytokine secretion from iPSC-RPE monolayers and 3D-oBRB  
737 tissues, apical and basal media were collected at 48-hour, 96-hour, and 2-week timepoints and frozen at -  
738 80°C until the assay was performed. Once thawed, the samples were centrifuged at 1400 RPM for 5 minutes  
739 to remove possible cell debris from sample supernatant. The assay was carried out using a Milliplex MAP  
740 Kits per the manufacturer's instructions (Millipore-Sigma, Cat# HCYTOMAG-60K) analyzed at the NIH  
741 Flow Cytometry Core Facility.

742 **Vascular Density Quantification:** 3D reconstruction of tissues was conducted on confocal images taken  
743 with 20x or 25x magnification, and area fractions of CD31 expression were calculated in each focal plane.  
744 For estimating distance from RPE region, beginning focal plane of vasculature was manually determined  
745 by comparing to z-stack images with ZO-1 expression by RPE. Thresholding was performed on z-stack  
746 images of the CD31 channel by Otsu thresholding method in ImageJ. Step size of the distance from RPE  
747 was determined as 5  $\mu\text{m}$  to adjust z-step size differences between samples.

748 **Quantification of Extracellular Matrix Deposition:** RPE monoculture and 3D-oBRB tissues in 24  
749 transwell plates were fixed with 4% PFA after 5 weeks from RPE seeding on transwell membrane or  
750 bioprinted “choroid”. The z-stacks of confocal images from the apical side of RPE to the basal side of RPE

751 were taken with the same microscope settings among the treatment groups. Mean intensity of Elastin and  
752 Collagen IV expression were measured using Image J.

753

#### 754 **Single cell RNA sequencing**

755 **Endothelial cell Isolation from 3D-oBRB tissues:** The endothelial isolation was performed by digesting  
756 the 3D-oBRB tissues. The digestion solution was created using 1.5 mg/mL Collagenase II (Gibco, Cat#  
757 17101-015), 0.5 mg/mL DNase I (Worthington Biochemical Corporation, Cat# 54D14897, Lakewood, NJ)  
758 and 0.2 mg/mL Dispase I (Sigma, Cat# D4818) in PBS. Tissues were removed with a sterile scalpel, placed  
759 in a 50 mL conical tube. Digestion solution was added (approximately 10 mL/6 tissues) and the samples  
760 were rocked on an orbital shaker at 37°C for 30 minutes. Following the incubation, the suspension is given  
761 20mL of media and is then centrifuged at 1000 RPM for 5 minutes. Endothelial cells were then purified  
762 using magnetic assisted cell sorting (Miltenyl Biotec, Cat# 130-042-401) protocol supplied by Miltenyl  
763 Biotec, counted, and analyzed with assistance from the NCATS Stem Cell Translation Laboratory.

764 **Single-cell RNA Library Preparation:** Single-cell suspensions were loaded on a Chromium Controller  
765 (10X Genomics) to generate single-cell gel bead-in-emulsions (GEMs) and barcoding. GEMs were  
766 transferred to PCR 8-tube strips, and GEM-reverse transcription was performed in a C1000 Touch Thermal  
767 Cycler (BioRad). GEMs were lysed in recovery buffer, and single-stranded cDNA was cleaned up using  
768 silane DynaBeads (Thermo Fisher Scientific). cDNA was amplified in a C1000 Touch Thermal Cycler  
769 (BioRad). Amplified cDNA was cleaned up using the SPRIselect Reagent (Beckman Coulter). Post cDNA  
770 amplification QC and quantification were done using a High Sensitivity D5000 ScreenTape Assay (Agilent)  
771 on a 4200 TapeStation System (Agilent). Library Construction was done by fragmentation at 32 °C for 5  
772 min, end repair, and A-tailing at 65 °C for 30 min. Post fragmentation, end repair, and A-tailing double-  
773 sided size selection were done using the SPRIselect Reagent (Beckman Coulter). Adaptor ligation was done  
774 at 20 °C for 15 min. Post ligation cleaned up using the SPRIselect Reagent (Beckman Coulter). Sample

775 indexing was done using the i7 Sample Index Plate (Chromium) in a C1000 Touch Thermal Cycler  
776 (BioRad). Post sample index PCR double sided size selection done using the SPRIselect Reagent (Beckman  
777 Coulter). Post library construction quantification was done using a High Sensitivity D1000 ScreenTape  
778 Assay (Agilent) on a 4200 TapeStation System (Agilent). Sequencing libraries were quantified by  
779 quantitative PCR using the KAPA library quantification kit for Illumina platforms (KAPA Biosystems) on  
780 a QuantStudio 12K Flex Real-Time PCR System (Thermo Fisher Scientific). Libraries were loaded on an  
781 Illumina HiSeq 3000 using the following: 98bp Read1, 8bp i7 Index, and 26bp Read2.

782 The cellranger software package from 10X Genomics, Inc. (version 3.0.1) was used to process raw BCL  
783 files from single-cell sequencing as follows. This work used the computational resources of the NIH HPC  
784 Biowulf cluster (<http://hpc.nih.gov>). Demultiplexing and FASTQ generation were done with the mkfastq  
785 command, and the count command created gene expression matrices. Dense matrices were created with the  
786 mat2csv command. Embryonic stem cell and iPSC lines were analyzed in the Seurat R package (Stuart et  
787 al. 2018 <https://www.biorxiv.org/content/10.1101/460147v1>; Seurat 2.3.4; R 3.5.2). Further data  
788 visualizations were made in R and with the ggplot2 package (3.1.0) (Table S2). Gene set enrichment  
789 analysis was performed using GSEA v4.0.3 (Broad Institute, Inc., MIT), the gene set databases C2 and C5  
790 (MSigDB v6.2), which are the curated and Gene Ontology sets, and EnrichR<sup>20</sup>. Endothelial and RPE single  
791 cell RNA-Seq phenotypes for 2D vs 3D-oBRB cells were coded as 0 and 1 respectively for a test of  
792 enrichment by ranked differential gene expression. Significantly enriched phenotypes were selected based  
793 on whether there was a nominal P value of  $< 0.5$  and a false discovery rate  $< 25\%$  between 2D and 3D-  
794 oBRB datasets. Log<sub>2</sub> ratio of classes was used for the ranking metric and otherwise default parameters were  
795 used. When comparing cytokine gene expression levels to cytokine detection levels in media, we extracted  
796 expression data was extracted for gene symbols that corresponded to the Luminex cytokine detection  
797 Assays performed previously. Only apical media was considered in these results. Only RPE gene expression  
798 data was considered in these results.

799

## 800 **Single cell RNAseq Analysis**

801 **Gene List Construction:** The ECM gene list was created by finding the gene ontology annotation for  
802 “extracellular matrix” ( <http://www.informatics.jax.org/go/term/GO:0031012>), then narrowing that list to  
803 those genes that are also RPE characteristic genes<sup>27</sup> and genes found in the CYCLOPS database<sup>22</sup> to be  
804 expressed in the tissues “RPE fetal” and “RPE adult” at levels >2x levels that were found in at least 70  
805 other tissues in the database. Selected genes must also exceed a minimum TPM threshold of 100. Afterward,  
806 the gene list was reduced to those pertaining to ECM proteins, matrix metalloproteinases, tissue-inhibitor  
807 matrix metalloproteinases, and ECM crosslinking proteins. Endothelial cell signature genes were derived  
808 from literature searches related to choroidal maturation<sup>21</sup>, arterial and venous specification<sup>19</sup>, as well as  
809 angiogenesis<sup>23</sup>.

810 **PCA Cluster Analysis:** Statistical comparisons between 2D and 3D-oBRB gene expression and Gene  
811 Enrichment analysis were performed in RStudio using the Seurat Gene Expression Analysis Package) and  
812 EnrichR. Single Cell samples were filtered to exclude samples with less than 200 unique RNA features,  
813 more than 6,000 unique RNA features, and more than 5% mitochondrial genome content. Afterward,  
814 samples were clustered using PCA (15 principal components analyzed) followed by tSNE. Endothelial cell  
815 clusters were identified using the Louvain algorithm at 0.2 resolution and RPE cell clusters were identified  
816 using 0.6 resolution. Gene enrichment was determined using the FindAllMarkers Seurat function. Genes in  
817 clusters with greater than 1.5-fold upregulation over the cell population average were processed in EnrichR  
818 to identify enriched biological processes (GO Biological Process 2018). Biological processes in clusters  
819 did not have 25 sufficiently upregulated genes were determined using comparisons with similar culture  
820 formats (i.e. 2D vs 2D or 3D-oBRB vs 3D-oBRB) only.

## 821 **Statistical Analysis**

822 All the data analyzed were unpaired (that is, the samples were independent from each other). Before  
823 conducting multiple comparison tests, the Brown–Forsythe test was performed to determine the  
824 homogeneity of variance between the datasets. One-way and Two-way ANOVA was performed prior to  
825 any post-hoc statistical comparison. To compare multiple datasets, Tukey’s multiple comparisons test was

826 used as a single-step multiple comparison procedure to find means significantly different from each other.  
827 The Bonferroni post-hoc test was used to detect significant differences in the Line-Probe Angiogenesis  
828 quantifications. To compare datasets with a vehicle control, Dunnett's test was used to find means  
829 significantly different from the control. Student's T-Test was used to find significant differences between  
830 two single conditions. All statistical tests were two-tailed (two-sided tests). All statistical analyses were  
831 performed using Graphpad Prism version 8.2.0 for Windows (GraphPad Software, San Diego, CA) or  
832 Microsoft® Excel® for Microsoft 365 MSO (16.0.13001.20266) 32-bit (Microsoft, Redmond, WA).  $P <$   
833 0.05 was considered significant. Variances between each group of data were represented by the standard  
834 deviation unless otherwise stated. Each statistical analysis method was indicated in individual quantification  
835 sections. Comparisons between ANG-1 and treated and non-treated conditions were performed using  
836 individual Sidak's Multiple Comparisons Tests on the day 4, 6, and 8 timepoints. Statistical comparisons  
837 between 2D and 3D-oBRB cytokine detection were performed using Sidak's Multiple Comparisons Test  
838 for each assayed gene. Calculations were performed using Graphpad Prism ver. 8.2.0 (GraphPad Software,  
839 Inc). Sample sizes to ensure adequate power were as follows: initial angiogenesis formation between printed  
840 structures,  $n = 5$  tissue replicates; ANG-1 modulating angiogenesis,  $n = 4$  tissue replicates;  
841 Immunofluorescence of ECM proteins,  $n = 3$ ; Outer-BRB maturation by RPE and printed choroid,  $n = 3$   
842 tissue replicates; Bevacizumab treatment on choroidal neovascularization model,  $n = 3$  tissue replicates per  
843 condition; APOE deposition and dry AMD,  $n = 3$  tissue replicates per condition; Single Cell RNASeq,  $n =$   
844 3012 2D RPE cells,  $n = 4380$  3D-oBRB RPE cells,  $n = 5369$  2D Endothelial cells,  $n = 1294$  3D-oBRB  
845 Endothelial cells. Samples were excluded from analysis if they were determined to be outliers through  
846 Grubbs' outlier test.

#### 847 **Data availability**

848 The authors declare that all data supporting the findings of this study are available within the article and its  
849 Supplementary Information files or are available from the corresponding author upon request.

850

851 **References**

- 852 1 Wong, W. L. *et al.* Global prevalence of age-related macular degeneration and disease burden  
853 projection for 2020 and 2040: a systematic review and meta-analysis. *Lancet Glob Health* **2**, e106-  
854 116, doi:10.1016/S2214-109X(13)70145-1 (2014).
- 855 2 McLeod, D. S. *et al.* Relationship between RPE and choriocapillaris in age-related macular  
856 degeneration. *Invest Ophthalmol Vis Sci* **50**, 4982-4991, doi:10.1167/iovs.09-3639 (2009).
- 857 3 Bhutto, I. & Luty, G. Understanding age-related macular degeneration (AMD): relationships  
858 between the photoreceptor/retinal pigment epithelium/Bruch's membrane/choriocapillaris  
859 complex. *Mol Aspects Med* **33**, 295-317, doi:10.1016/j.mam.2012.04.005 (2012).
- 860 4 Song, M. J. & Bharti, K. Looking into the future: Using induced pluripotent stem cells to build two  
861 and three dimensional ocular tissue for cell therapy and disease modeling. *Brain Res* **1638**, 2-14,  
862 doi:10.1016/j.brainres.2015.12.011 (2016).
- 863 5 Farecki, M. L. *et al.* Characteristics of type 1 and 2 CNV in exudative AMD in OCT-Angiography.  
864 *Graefes Arch Clin Exp Ophthalmol* **255**, 913-921, doi:10.1007/s00417-017-3588-y (2017).
- 865 6 Kovach, J. L., Schwartz, S. G., Flynn, H. W., Jr. & Scott, I. U. Anti-VEGF Treatment Strategies for Wet  
866 AMD. *J Ophthalmol* **2012**, 786870, doi:10.1155/2012/786870 (2012).
- 867 7 Barben, M., Samardzija, M. & Grimm, C. The Role of Hypoxia, Hypoxia-Inducible Factor (HIF), and  
868 VEGF in Retinal Angiomatous Proliferation. *Adv Exp Med Biol* **1074**, 177-183, doi:10.1007/978-3-  
869 319-75402-4\_22 (2018).
- 870 8 Campbell, M. & Humphries, P. The blood-retina barrier: tight junctions and barrier modulation.  
871 *Adv Exp Med Biol* **763**, 70-84 (2012).
- 872 9 Nickla, D. L. & Wallman, J. The multifunctional choroid. *Prog Retin Eye Res* **29**, 144-168,  
873 doi:10.1016/j.preteyeres.2009.12.002 (2010).

874 10 Hoshino, A., Chiba, H., Nagai, K., Ishii, G. & Ochiai, A. Human vascular adventitial fibroblasts  
875 contain mesenchymal stem/progenitor cells. *Biochem Biophys Res Commun* **368**, 305-310,  
876 doi:10.1016/j.bbrc.2008.01.090 (2008).

877 11 Orlova, V. V. *et al.* Generation, expansion and functional analysis of endothelial cells and pericytes  
878 derived from human pluripotent stem cells. *Nat Protoc* **9**, 1514-1531,  
879 doi:10.1038/nprot.2014.102 (2014).

880 12 Sharma, R. *et al.* Clinical-grade stem cell-derived retinal pigment epithelium patch rescues retinal  
881 degeneration in rodents and pigs. *Sci Transl Med* **11**, doi:10.1126/scitranslmed.aat5580 (2019).

882 13 Shiihara, H. *et al.* Quantitative analyses of diameter and running pattern of choroidal vessels in  
883 central serous chorioretinopathy by en face images. *Sci Rep* **10**, 9591, doi:10.1038/s41598-020-  
884 66858-1 (2020).

885 14 Lamalice, L., Le Boeuf, F. & Huot, J. Endothelial cell migration during angiogenesis. *Circ Res* **100**,  
886 782-794, doi:10.1161/01.RES.0000259593.07661.1e (2007).

887 15 Maminishkis, A. *et al.* Confluent monolayers of cultured human fetal retinal pigment epithelium  
888 exhibit morphology and physiology of native tissue. *Invest Ophthalmol Vis Sci* **47**, 3612-3624,  
889 doi:10.1167/iovs.05-1622 (2006).

890 16 Campochiaro, P. A., Jerdon, J. A. & Glaser, B. M. The extracellular matrix of human retinal pigment  
891 epithelial cells in vivo and its synthesis in vitro. *Invest Ophthalmol Vis Sci* **27**, 1615-1621 (1986).

892 17 Choi, W. *et al.* Choriocapillaris and choroidal microvasculature imaging with ultrahigh speed OCT  
893 angiography. *PLoS One* **8**, e81499, doi:10.1371/journal.pone.0081499 (2013).

894 18 Grebe, R. *et al.* Ultrastructural analysis of submacular choriocapillaris and its transport systems in  
895 AMD and aged control eyes. *Exp Eye Res* **181**, 252-262, doi:10.1016/j.exer.2019.02.018 (2019).

896 19 dela Paz, N. G. & D'Amore, P. A. Arterial versus venous endothelial cells. *Cell Tissue Res* **335**, 5-16,  
897 doi:10.1007/s00441-008-0706-5 (2009).

- 898 20 Kuleshov, M. V. *et al.* Enrichr: a comprehensive gene set enrichment analysis web server 2016  
899 update. *Nucleic Acids Res* **44**, W90-97, doi:10.1093/nar/gkw377 (2016).
- 900 21 Songstad, A. E. *et al.* Generating iPSC-Derived Choroidal Endothelial Cells to Study Age-Related  
901 Macular Degeneration. *Invest Ophthalmol Vis Sci* **56**, 8258-8267, doi:10.1167/iovs.15-17073  
902 (2015).
- 903 22 Swamy, V. & McGaughey, D. Eye in a Disk: eyeIntegration Human Pan-Eye and Body  
904 Transcriptome Database Version 1.0. *Invest Ophthalmol Vis Sci* **60**, 3236-3246,  
905 doi:10.1167/iovs.19-27106 (2019).
- 906 23 Zanutelli, M. R. *et al.* Stable engineered vascular networks from human induced pluripotent stem  
907 cell-derived endothelial cells cultured in synthetic hydrogels. *Acta Biomater* **35**, 32-41,  
908 doi:10.1016/j.actbio.2016.03.001 (2016).
- 909 24 Curcio A.C, J. M. in *Retina* Vol. Vol. 1, Part 2: Basic Science and Translation to Therapy, (ed Srinivas  
910 R. Sadda Stephen J. Ryan, David R. Hinton, Andrew P. Schachat, Srinivas R. Sadda, C.P. Wilkinson,  
911 Peter Wiedemann, Andrew P. Schachat) Ch. 20, 465-481 (London: Elsevier. 5th ed., 2013).
- 912 25 Michaelides, M., Hunt, D. M. & Moore, A. T. The genetics of inherited macular dystrophies. *J Med*  
913 *Genet* **40**, 641-650, doi:10.1136/jmg.40.9.641 (2003).
- 914 26 Corominas, J. *et al.* Whole-Exome Sequencing in Age-Related Macular Degeneration Identifies  
915 Rare Variants in COL8A1, a Component of Bruch's Membrane. *Ophthalmology* **125**, 1433-1443,  
916 doi:10.1016/j.ophtha.2018.03.040 (2018).
- 917 27 Miyagishima, K. J. *et al.* In Pursuit of Authenticity: Induced Pluripotent Stem Cell-Derived Retinal  
918 Pigment Epithelium for Clinical Applications. *Stem Cells Transl Med* **5**, 1562-1574,  
919 doi:10.5966/sctm.2016-0037 (2016).
- 920 28 Booij, J. C., Baas, D. C., Beisekeeva, J., Gorgels, T. G. & Bergen, A. A. The dynamic nature of Bruch's  
921 membrane. *Prog Retin Eye Res* **29**, 1-18, doi:10.1016/j.preteyeres.2009.08.003 (2010).

922 29 Strunnikova, N. V. *et al.* Transcriptome analysis and molecular signature of human retinal pigment  
923 epithelium. *Hum Mol Genet* **19**, 2468-2486, doi:10.1093/hmg/ddq129 (2010).

924 30 Anderson, D. H. *et al.* Local cellular sources of apolipoprotein E in the human retina and retinal  
925 pigmented epithelium: implications for the process of drusen formation. *Am J Ophthalmol* **131**,  
926 767-781, doi:10.1016/s0002-9394(00)00961-2 (2001).

927 31 Johnson, L. V. *et al.* Cell culture model that mimics drusen formation and triggers complement  
928 activation associated with age-related macular degeneration. *Proc Natl Acad Sci USA* **108**, 18277-  
929 18282, doi:10.1073/pnas.1109703108 (2011).

930 32 Vadlapatla, R. K., Vadlapudi, A. D. & Mitra, A. K. Hypoxia-inducible factor-1 (HIF-1): a potential  
931 target for intervention in ocular neovascular diseases. *Curr Drug Targets* **14**, 919-935,  
932 doi:10.2174/13894501113149990015 (2013).

933 33 Mammadzada, P., Corredoira, P. M. & Andre, H. The role of hypoxia-inducible factors in  
934 neovascular age-related macular degeneration: a gene therapy perspective. *Cell Mol Life Sci* **77**,  
935 819-833, doi:10.1007/s00018-019-03422-9 (2020).

936 34 Chilov, D. *et al.* Induction and nuclear translocation of hypoxia-inducible factor-1 (HIF-1):  
937 heterodimerization with ARNT is not necessary for nuclear accumulation of HIF-1alpha. *J Cell Sci*  
938 **112 ( Pt 8)**, 1203-1212 (1999).

939 35 Wavre-Shapton, S. T., Tolmachova, T., Lopes da Silva, M., Futter, C. E. & Seabra, M. C. Conditional  
940 ablation of the choroideremia gene causes age-related changes in mouse retinal pigment  
941 epithelium. *PLoS One* **8**, e57769, doi:10.1371/journal.pone.0057769 (2013).

942 36 Huang, J. D., Presley, J. B., Chimento, M. F., Curcio, C. A. & Johnson, M. Age-related changes in  
943 human macular Bruch's membrane as seen by quick-freeze/deep-etch. *Exp Eye Res* **85**, 202-218,  
944 doi:10.1016/j.exer.2007.03.011 (2007).

- 945 37 Spilsbury, K., Garrett, K. L., Shen, W. Y., Constable, I. J. & Rakoczy, P. E. Overexpression of vascular  
946 endothelial growth factor (VEGF) in the retinal pigment epithelium leads to the development of  
947 choroidal neovascularization. *Am J Pathol* **157**, 135-144, doi:10.1016/S0002-9440(10)64525-7  
948 (2000).
- 949 38 Sun, L. *et al.* Advanced glycation end products promote VEGF expression and thus choroidal  
950 neovascularization via Cyr61-PI3K/AKT signaling pathway. *Sci Rep* **7**, 14925, doi:10.1038/s41598-  
951 017-14015-6 (2017).

952

# Figures

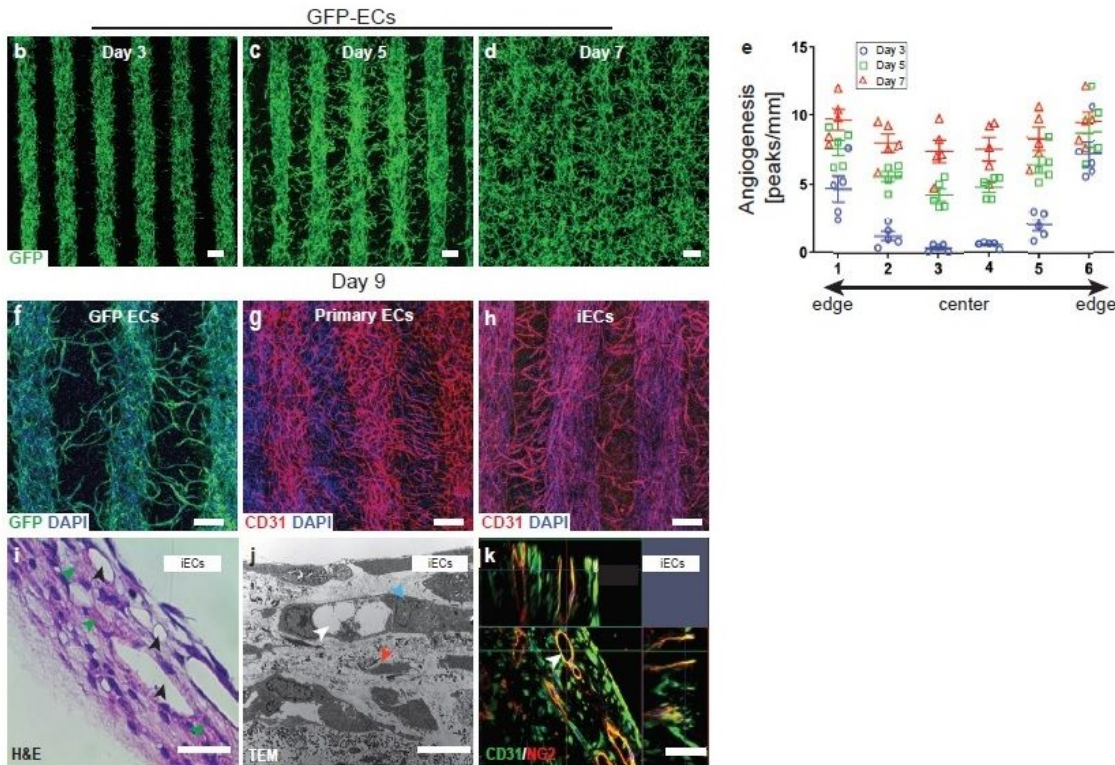
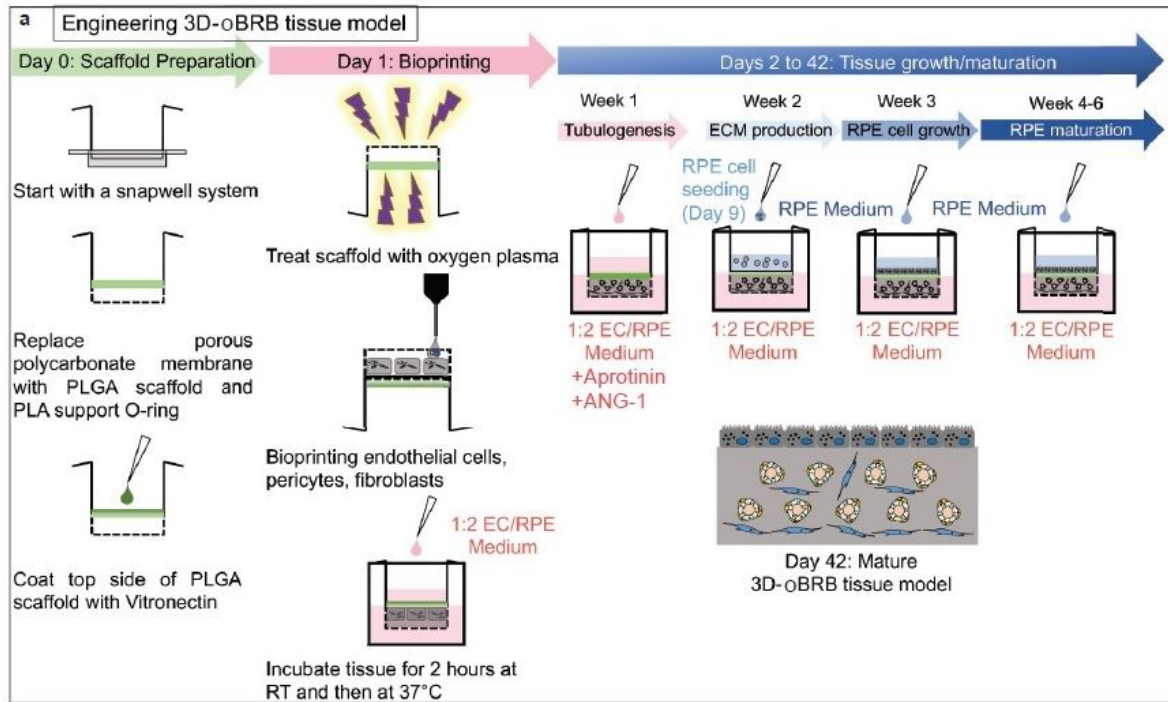


**Figure 1**

Design of 3D-oBRB. a, Bioprinting workflow with 93 human endothelial cells (ECs) and RPE. b-d, Vascular development of GFP expressing primary ECs on day 3 (a), day 5 (b) and day 7 (c) after printing. Scale bars, 500  $\mu$ m. e, Angiogenesis between printed stripes (n=5). #p<0.05 in day 3 vs. day 5,  $\dagger$ p<0.05 in day 5

vs. day 7, \* $p < 0.05$  in day 3 vs. day 7. f-h, Vascular formation of GFP-positive ECs (green, f), primary ECs (CD31 - red, g), and iPSC-derived ECs (iECs, CD31 - red, h) and nuclei (blue). Scale bars, 500  $\mu\text{m}$ . i, H&E images of 10  $\mu\text{m}$  thick cross section of iECs derived vascular tissue (day 7). Vasculature is marked with black arrowheads, and ECM components are marked with green arrowheads. Scale bar, 50  $\mu\text{m}$ . j, Transmission electron microscope (TEM) images of iECs derived vascular tissue at day 7. White arrowhead shows a capillary, blue arrowhead marks pericytes, and red arrowhead labels fibroblasts. Scale bar, 300 nm. k, Orthogonal views of confocal images of 100  $\mu\text{m}$  thick tissue sections stained with CD31 (ECs; green) and NG2 (pericytes; red). White arrowheads mark patent EC-derived capillaries. Scale bar, 50  $\mu\text{m}$ . Statistical significance was attributed to values of  $p < 0.05$  as determined by two-way ANOVA and Bonferroni post-hoc pair comparison. All error bars indicate STE.

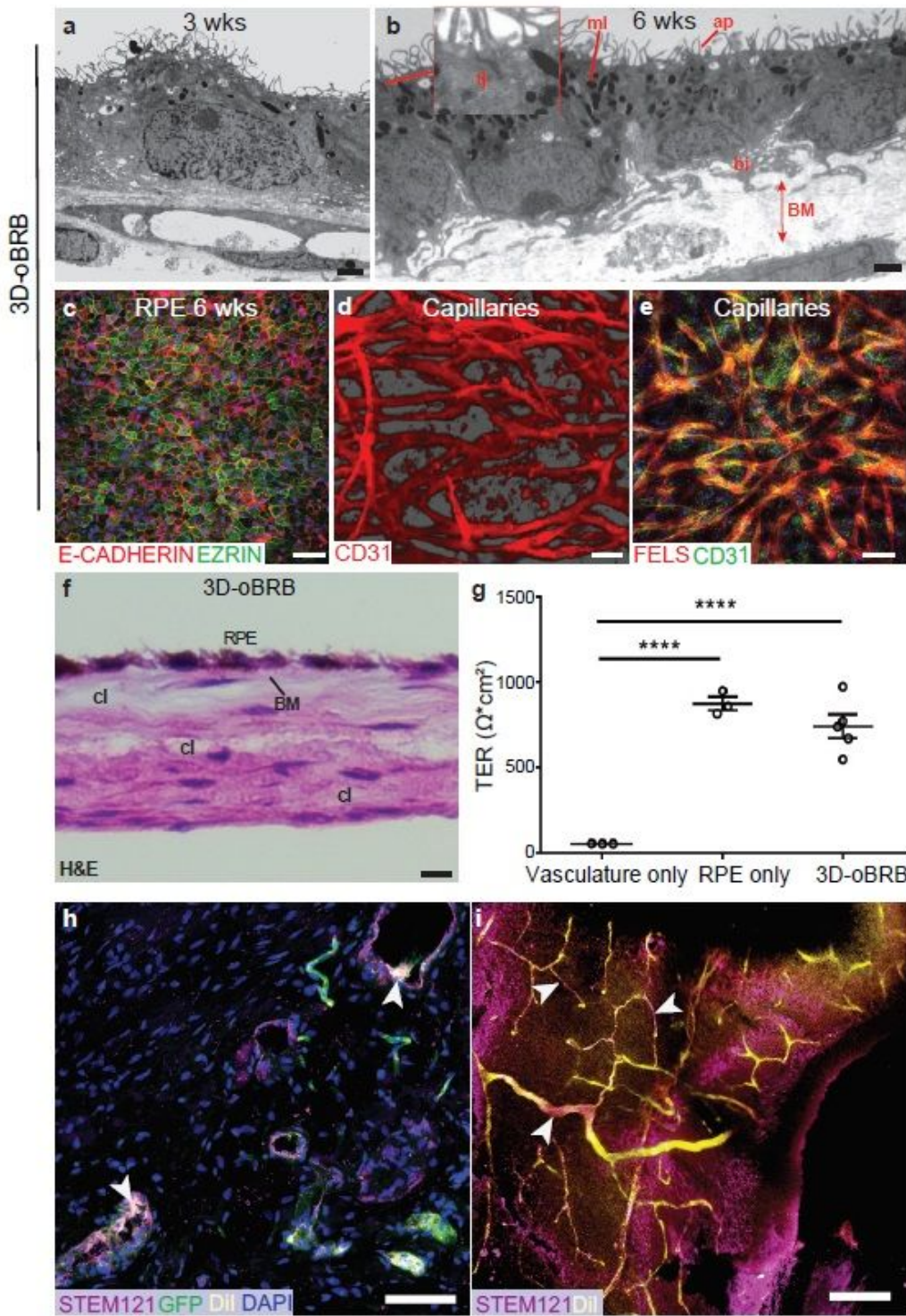


**Figure 2**

Engineering of 3D oBRB. a,b, TEM images 209 of 3D-oBRB maturity at week 3 (a) and 6 (b) with RPE pigmentation: melanin (ml), RPE apical processes (ap), RPE basal infoldings (bl), tight junction (tj) formation and Bruch's membrane (BM). Scale bars, 1  $\mu\text{m}$  (a), 2  $\mu\text{m}$  (b) (n=3) c, Immunostaining for RPE maturity markers E-CADHERIN (red) and EZRIN (green) in 6-week-old tissues. Scale bar, 50  $\mu\text{m}$ . d, 3D rendered image of CD31 (red) immunostained capillary-bed in 6-week-old 3D-oBRB. Scale bar, 50  $\mu\text{m}$ .

(n=4) e, Immunostaining for capillary-maturation marker FELS (red) co-labeled with EC marker CD31 (green) of confocal images of vascular networks labeled with CD31 (red). Scale bar, 50µm. (n=3) f, H&E staining of 6-week-old tissues containing capillaries (cl), RPE, and Bruch's membrane (BM). Scale bar, 10 µm. g, Transepithelial resistance (TER) of 3D-oBRB compared to vascular and 2D-RPE (n=3). h, GFP signal in human ECs and immunostaining with STEM121 (magenta) detect human capillaries that are perfused with Dil (yellow) in 10 µm cryosections of rat choroid transplanted with 3D-oBRB. Scale bar 75 µm. (n=8 eyes from 4 animals). i, Immunostaining for STEM121 (magenta) detects human capillaries integrated with rat capillaries detected by Dil (yellow) perfusion in 100 µm vibratome sections of transplanted rat choroid. Scale bar 100 µm. Statistical significance was attributed to values of  $p < 0.05$  as determined by one-way ANOVA with Tukey's multiple-comparisons test. \*\*\*\* $p < 0.0001$ , All error bars indicate STE.

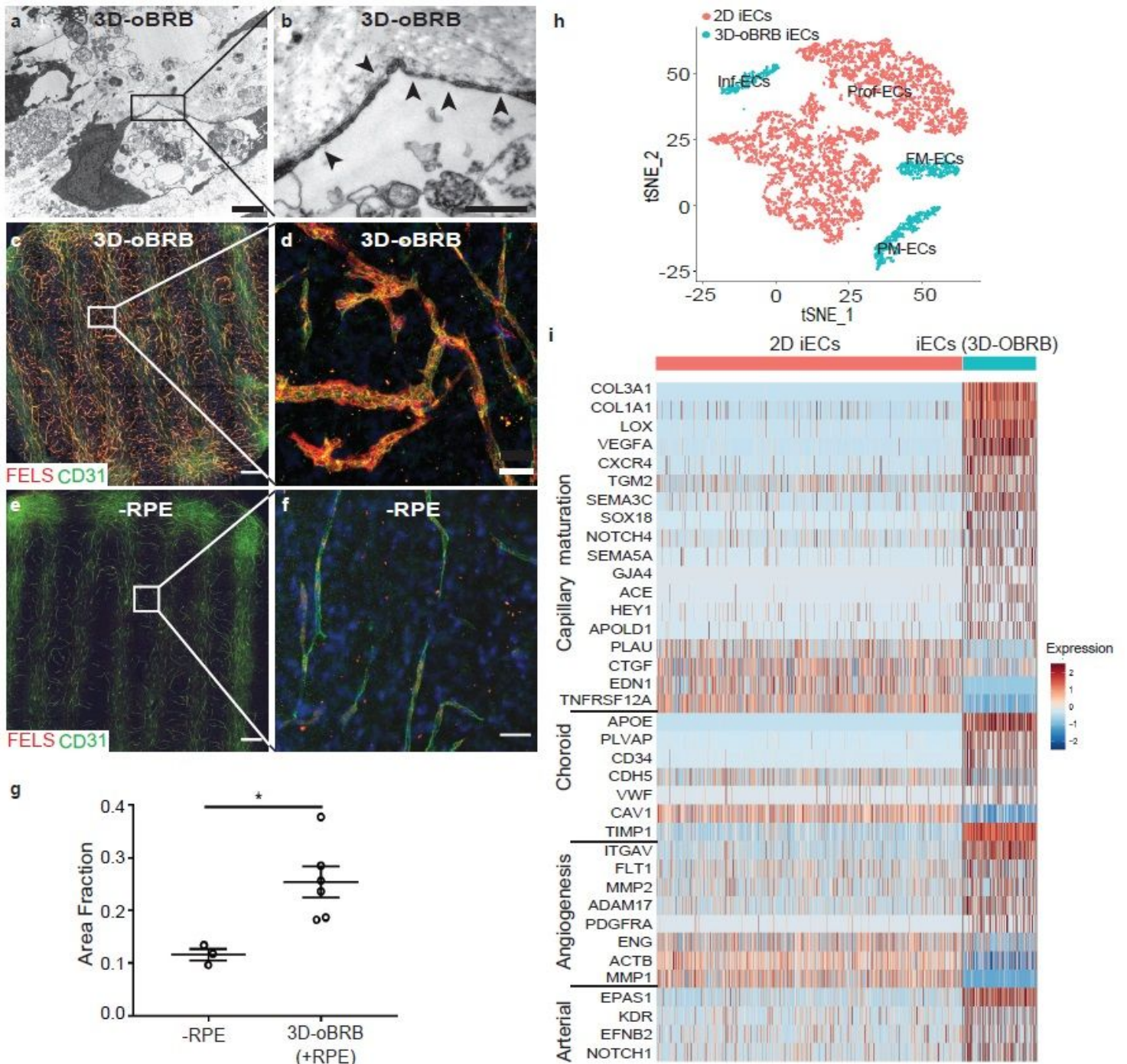


**Figure 3**

Capillary maturation in 277 3D-oBRB. a,b, TEM images highlight fenestration (arrowheads) in iECs with in 3D-oBRB capillaries at week 6. Scale bars, 2  $\mu\text{m}$  (a), 500 nm (b). (n=3). c-f, Immunostaining for FELS (red) and CD31 (green) in 3D-oBRB (with RPE; c, d) or just the vasculature (without RPE; e, f). Scale bars, 500  $\mu\text{m}$  (c, e) and 50  $\mu\text{m}$  (d, f). g, Area fraction of FELS and CD31 expression in vascular regions with or without RPE. (n=3). h, TSNE plots from sc-RNA seq of 2D iECs and iECs from 3D-oBRB. i, Gene expression differences between 2D iECs and iECs from 3D-oBRB for genes related to endothelial maturation, choroid, angiogenesis, and arterial development. Statistical significance was attributed to values of  $P < 0.05$  as

determined by unpaired t-test. Data depicts results from n = 3012 cells (2D RPE), n = 4380 cells (3D-oBRB RPE), n = 5369 cells (2D iECs), and n = 1294 cells (3D-OBRB iECs). \*p<0.05, All error bars indicate STE.

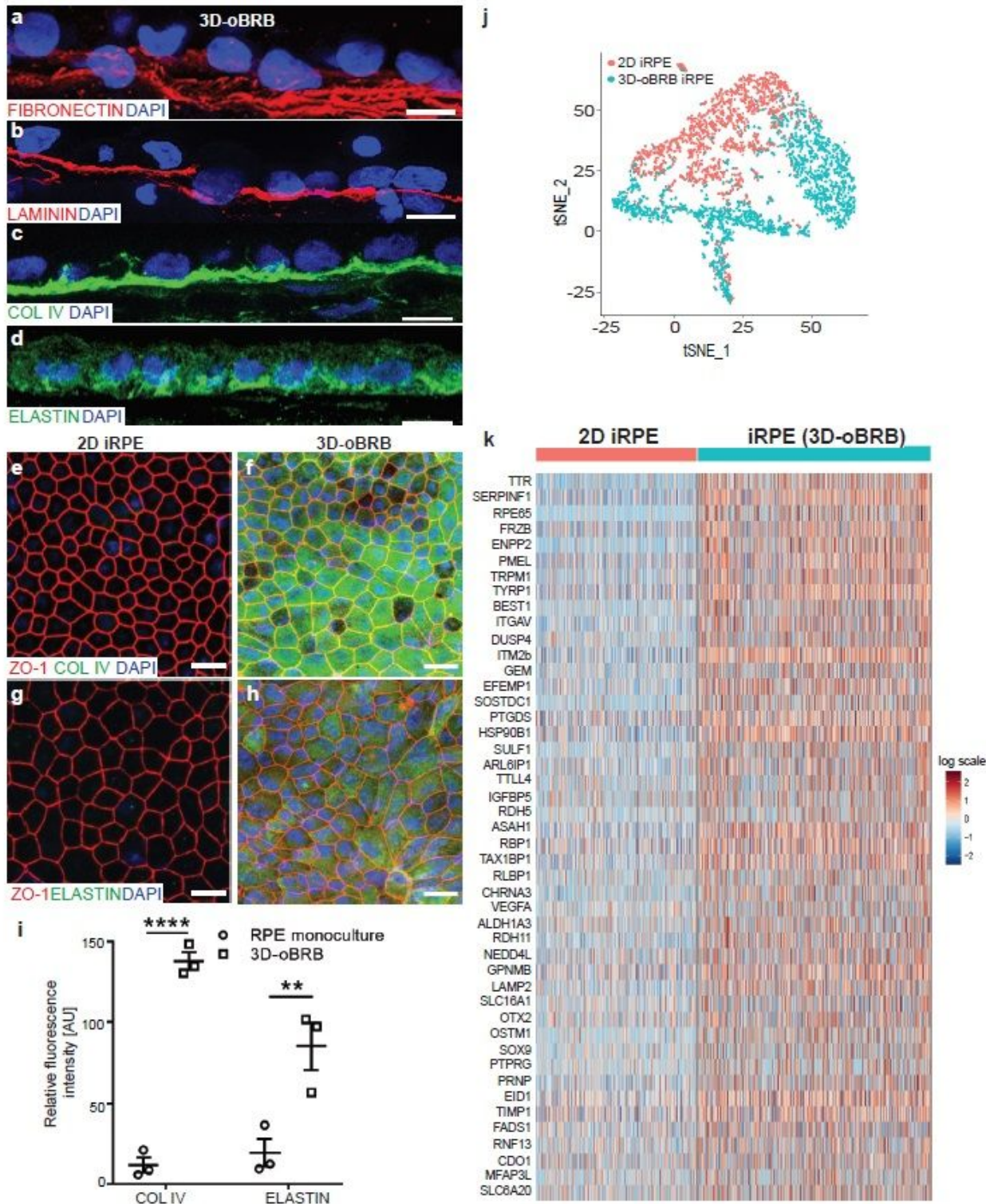


**Figure 4**

RPE maturity in 3D-oBRB. a-d, Cross sections of 3D-oBRB immunostained for Bruch's membrane proteins FIBRONECTIN (a), LAMININ (b), COLLAGEN IV (COL IV) (c), and ELASTIN (d). Nuclei stained with DAPI. Scale bars, 10µm. e-h, 2D RPE monoculture (e, g) and 3D-oBRB (f, h), co immunostained for COL IV

(green) or ELASTIN with ZO-1 (red), and nuclei (blue). Scale bars, 30  $\mu\text{m}$ . i, Fluorescence mean intensity comparison of ELASTIN and COL IV immunostaining in 2D-iRPE and 3D oBRB models. (n=3). j, tSNE plots from sc-RNA seq of 2D-iRPE and RPE in 3D-oBRB. k, Gene expression of RPE signature genes, comparison between 2D-iRPE and RPE in 3D-oBRB. Statistical significance was attributed to values of  $p < 0.05$  as determined by two-way ANOVA and Sidak's multiple comparison test. \*\* $p < 0.01$ , \*\*\*\* $p < 0.0001$ . All error bars indicate STE.

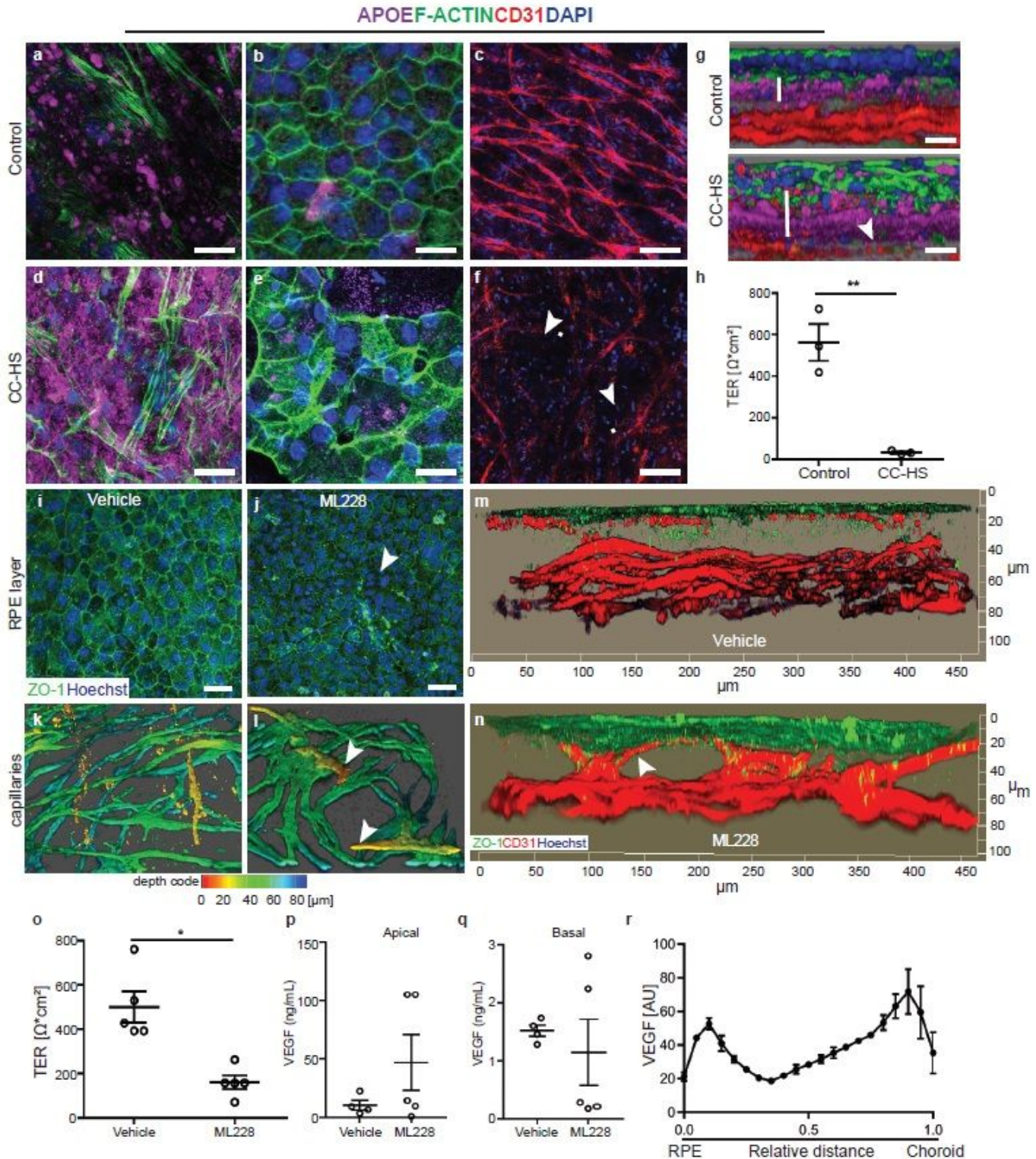
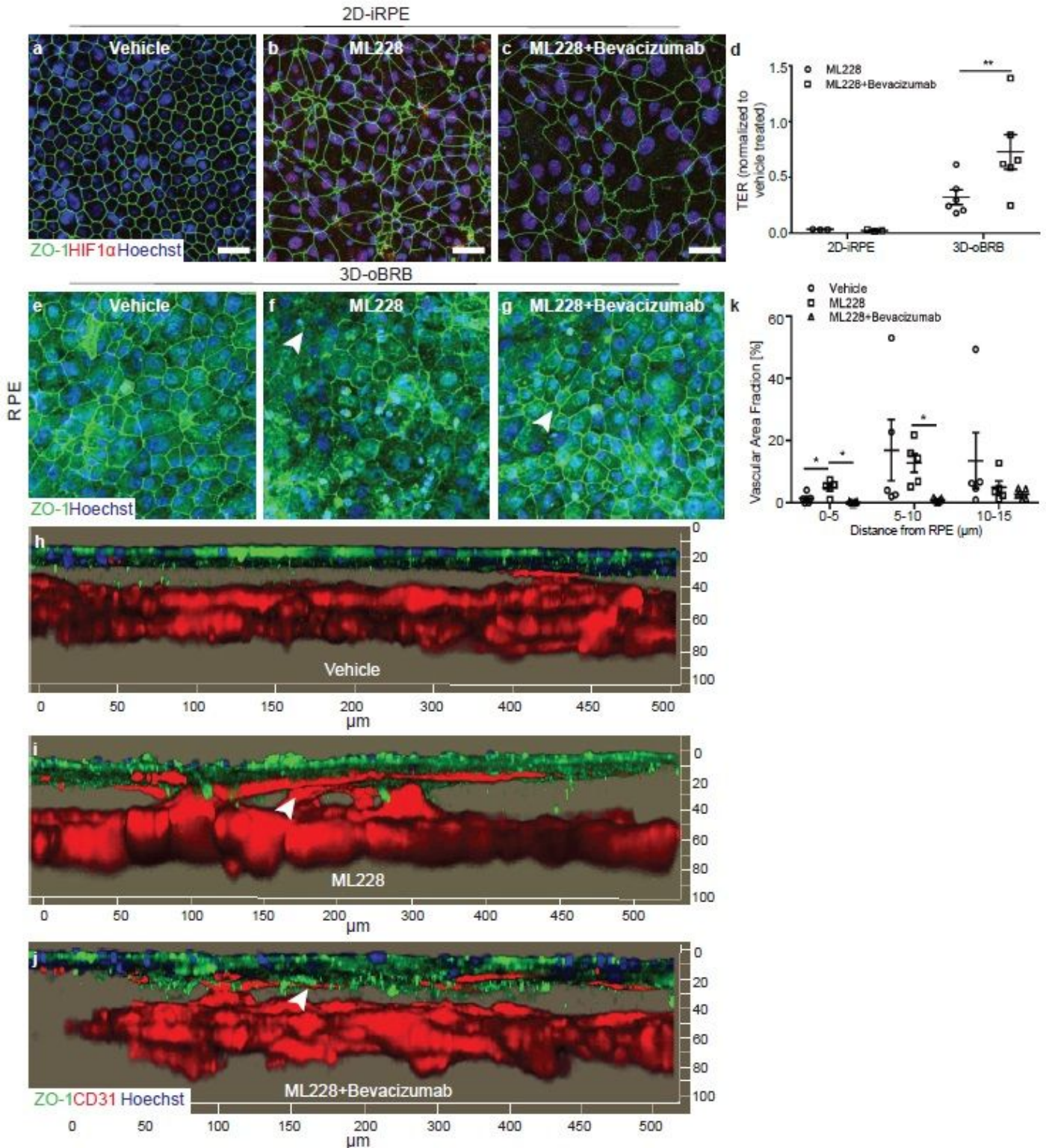


Figure 5

RPE dependent 392 choroid degeneration in dry and wet AMD models of 3D-oBRB. a-g, En face (a-f), cross-section (g) views of APOE (magenta), CD31 (red) immunostaining, F-ACTIN (green), Hoechst (blue) in complement competent human serum (CC-HS) treated and control 3D-oBRB. Arrowheads mark degenerated RPE and capillaries. Scale bars, 100µm. (g) white vertical lines mark Bruch's membrane. Scale bars, 10µm. (n=3) h, TER of control and CC-HS treated 3D-oBRB (n=3). i,j, Confocal images of RPE from 3D-oBRB, immunostained with ZO-1 (green) and Hoechst (blue). Arrowhead marks lost ZO-1 signal. Scale bars, 30 µm. k,l, Depth code of 3D reconstructed confocal images. Color gradient along z-axis (100 µm depth) starting from subRPE zone (red) to the end of choroid (blue); in vehicle-treated 3D-oBRB (k) and in ML228 treated 3D-oBRB (l). Arrowheads mark capillaries in the sub-RPE region. Scale bars, 100 µm. m,n, Side view images of CNV, immunostained with ZO-1 (green) and CD31(red). Scale in x-axis, 50µm and in z-axis, 10µm. i-n, (n=5) o, TER measurement on vehicle or ML228 treated 3D-oBRB (n=5). p, q apical (p) and basal (q) VEGF secretion in vehicle and ML228 treated 3D-oBRB (n=4). r, Fluorescence intensity of VEGF staining in cryosectioned 3D-oBRB tissue slice. Quantification of subRPE region (0.0 fractional distance) to the bottom of the choroid layer (1.0 fractional distance) (n=3). Statistical significance was attributed to values of  $p < 0.05$  as determined by paired t-test (o,p,q) or two-way ANOVA and Sidak's multiple comparison test (g,h). \* $p < 0.05$ , \*\*\* $p < 0.001$ , \*\*\*\* $p < 0.0001$ . All error bars indicate STE 408 (g,o,p,q,r).



**Figure 6**

Bevacizumab treatment suppresses 438 wet-AMD in 3D-oBRB. a-c, RPE monoculture at 2 weeks treated with DMSO as a vehicle control (a), ML228 (2μM) (b), and ML228 (2μM)+bevacizumab (0.284mg/ml) (c), immunostained for HIF-1α (red), ZO-1 (green), and nuclei stained with Hoechst (blue). Scale bars, 30μm. (n=3). d, TER measurement comparison between 2D-iRPE and 3D-oBRB for ML228 and ML228+bevacizumab treated samples. TER values were normalized to vehicle treated 3D-oBRBs. (2D-

iRPE, n=3; 3D-oBRB, n=6). e-g, Maximum intensity projection images of RPE of 3D-oBRB, immunostained with ZO-1 (green) and stained with Hoechst for nuclei (blue). Degenerated and recovered RPE are marked with arrowheads in (f and g). Scale bars, 25 $\mu$ m. h-j, Side view of 3D reconstructed images of vehicle (h), ML228 (i), and ML228+bevacizumab (j) treated 3D-oBRB tissues, immunostained with ZO-1 (green) and CD31 (red). Arrowheads in (i) mark hyperproliferating capillaries and in (j) mark retracted capillaries. Scale in x-axis, 50 $\mu$ m and in z-axis, 10 $\mu$ m. e-j, (n=4). k, Vascular area fraction was calculated from CD31 positive area in each z-stack. (n=5). Statistical significance was attributed to values of  $p < 0.05$  as determined by unpaired t-test (m) or two-way ANOVA and Sidak's multiple comparison test (d,h,l). \* $p < 0.05$ , \*\* $p < 0.01$ , \*\*\*\* $p < 0.0001$ . All error bars indicate STE.

## Supplementary Files

This is a list of supplementary files associated with this preprint. Click to download.

- [SupplementrayV1.mp4](#)
- [SupplementrayV2.mp4](#)
- [SupplementrayV3.mp4](#)
- [SupplementrayV4.mp4](#)
- [SupplementrayV5.mp4](#)
- [SupplementrayV6.mp4](#)
- [Supplementarytablesandfigures.pdf](#)
- [flatNMETHA44557Anreditorialpolicychecklist.pdf](#)
- [flatNMETHA44557Anreportingsummary.pdf](#)